

Department of Physics and Astronomy

University of Heidelberg

Bachelor thesis

in Physics

submitted by

Lukas Witola

born in Bonn

2016

**Commissioning of a test stand for quality
assurance of fibre modules using cosmic rays
for the SciFi detector upgrade**

This Bachelor thesis has been carried out by Lukas Witola

at the

Physikalisches Institut

under the supervision of

Prof. Dr. Stephanie Hansmann-Menzemer

Abstract:

During the LHC's long shutdown in 2018, the LHCb detector will be upgraded and the current tracking system will be replaced by the Scintillating Fibre Tracker. It will use 2.5m long and 250 μ m thick scintillating fibres, which are readout by silicon photomultipliers, to reconstruct particle trajectories. The fibres are arranged into mats of which eight form a module.

This thesis investigates whether quality assurance of the modules can be done with cosmic rays. In the first part the commissioning of the setup is described which involves calibrating the SiPMs to run at the same over voltage, and setting up a trigger system for the cosmic rays.

In the second part the setup is used to measure the light yield of a 1m long and a 2.5m long module. It is found that measurements with cosmic rays are consistent with measurements done using a β -source which is how the light yield is usually measured. Therefore cosmic rays can be used for quality assurance of fibre modules.

Due to the low rate of cosmic rays measurements need at least one or two days depending on the trigger geometry and efficiency.

Zusammenfassung:

Es ist geplant, während der Wartungsarbeiten am LHC im Jahr 2018, das bisherige Tracking System des LHCb Detektors durch den Scintillating Fibre Tracker zu ersetzen. Der Tracker besteht aus 2.5m langen und 250 μ m dicken szintillierenden Fasern, die von Silizium-Photomultipliern (SiPM) ausgelesen werden. Die Fasern werden zu Matten zusammengefasst, von denen jeweils acht ein Modul bilden.

In dieser Arbeit wird untersucht ob eine Qualitätskontrolle der Module mit kosmischer Strahlung möglich ist. Im ersten Teil der Arbeit wird die Inbetriebnahme des Versuchsaufbaus beschrieben. Diese umfasst die Kalibration der SiPMs sowie den Aufbau eines Trigger Systems für die kosmische Strahlung.

Im zweiten Teil der Arbeit wird mit dem Aufbau die Lichtausbeute eines 1m und eines 2,5m langen Moduls gemessen. Es zeigt sich, dass die Messergebnisse mit kosmischer Strahlung konsistent mit Messungen mit β -Strahlung sind. Es ist also möglich die Qualität der Module mit Hilfe kosmischer Strahlen zu überprüfen.

Aufgrund des geringen Flusses der Strahlung dauern die Messungen, abhängig von der Triggergeometrie, ein bis zwei Tage.

Contents

1	Introduction	7
2	The LHCb Experiment	9
2.1	The LHCb Detector	10
2.1.1	Vertex Locator	10
2.1.2	Magnet	10
2.1.3	RICH Detectors	11
2.1.4	Tracking System	11
2.1.5	Calorimeters	11
2.1.6	Muon System	11
2.2	The LHCb Upgrade	12
3	The Scintillating Fibre Tracker	13
3.1	Scintillating Fibres	14
3.2	Fibre Mats and Modules	15
3.3	Silicon Photomultipliers	17
3.3.1	Introduction to Semiconductivity	17
3.3.2	p-n-Junction	20
3.3.3	Working Principle of SiPMs	21
3.3.4	SiPM Characteristics	23
3.4	Readout Electronics	25
4	Experiment Setup	28
4.1	Calibration of the DAC Controlled DC-DC Converter	30
4.2	Delay Time Scan	30
5	SiPM Calibration	33
5.1	Calibration Routine	34
5.2	Calibration Results	36
6	Cosmic Rays	37
6.1	Primary Cosmic Rays	37
6.2	Secondary Cosmic Rays	38
7	Trigger Setup	40
7.1	Scintillation Counters	41
7.2	Electronics	41
7.2.1	Discriminators	42

7.2.2	Logic Units	42
7.2.3	Delay Unit	42
7.2.4	Scaler	43
7.2.5	NIM to TTL Converter	43
7.3	Adjusting the PMT Voltage	43
7.4	Adjusting the Discriminator Thresholds	45
7.5	Adjusting the Delay Time	46
7.6	Trigger Performance	47
7.7	Mechanical Installation	47
8	Light Yield Measurement	48
8.1	Analysis Method	48
8.2	Measurements of the 1m long Module	49
8.3	Measurements of the 2.5m long Module	53
8.3.1	Measurement with Cosmic Rays	53
8.3.2	Measurement with a β -Source	54
8.3.3	Measurement with Cosmic Rays and β -Source Trigger	56
9	Summary and Outlook	58
10	References	60
A	Appendix	62
A.1	Additional Figures	62

1 Introduction

The Standard Model of particle physics (SM) is an effective quantum field theory that was developed in the second half of the 20th century and extended until today. It describes all known elementary particles and their interactions with great success and until now has withstood all experimental tests. But still there are physical phenomena like dark matter or the neutrino mass which the SM fails to explain.

The Large Hadron Collider (LHC) located at the international research center CERN¹ near Geneva, Switzerland, is currently the world's most powerful ring accelerator reaching energies of 13TeV which provide the ideal environment to test the SM. Measurements are made by the four experiments ALICE, ATLAS, CMS, and LHCb.

The LHCb experiment specializes in studying B meson decays which allow to probe the SM with high precision. Since most of the measurement uncertainties are currently limited by statistics, the LHCb detector will be upgraded during the LHC's long shutdown in 2018. It then will be operated at a luminosity of $\mathcal{L} = 2 \cdot 10^{33} \text{cm}^{-2} \text{s}^{-1}$ which is five times the current value. The currently installed tracking system consists of three stations with an active area of $600\text{cm} \times 490\text{cm}$ each and uses two detector technologies: a silicon micro-strip Inner Tracker around the beam pipe and a straw drift tube Outer Tracker. Due to the increase in luminosity the Outer Tracker will not be able to handle the high occupancy and particle rate and, therefore, the whole tracking system will be replaced by the Scintillating Fibre Tracker (SciFi).

The SciFi tracker uses 2.5m long and 250 μm thick scintillating fibres to reconstruct particle trajectories. They will be read out by silicon photomultipliers (SiPM) which offer the needed granularity and spatial resolution. The detector consists of twelve layers arranged perpendicular to the beam pipe between 7.5m and 9.3m away from the nominal proton-proton interaction point. Each layer has an active area of $6.2\text{m} \times 5\text{m}$ and is made up of twelve modules. The modules measure $52\text{cm} \times 5\text{m}$ and are composed of six layers of scintillating fibres sandwiched between a lightweight honeycomb support structure.

During production of the modules it is crucial to perform quality checks to make sure their performance is uniform. This thesis investigates whether the quality control can be done using cosmic rays. It is structured as follows:

In Chapter 2 the current LHCb detector and the planned upgraded detector are presented. Chapter 3 then describes the SciFi detector in more detail focusing on the characteristics of the fibres, the SiPMs, and the readout electronics. After this introductory part the setup and commissioning of the quality assurance stand is described.

¹Conseil Européen pour la Recherche Nucléaire

In Chapter 4 the whole experiment setup is introduced and described in detail in the following chapters. Chapter 5 explains how to calibrate the SiPMs using a light injection system. This makes sure the electronic response of the test system is uniform. After giving an introduction to cosmic rays in Chapter 6, the commissioning of the trigger setup is described in Chapter 7. Using this setup two modules are investigated: a 1m long module which is known to have no considerable flaws and a full 2.5m long module with several known damages. The results are presented in Chapter 8, and summarized in Chapter 9.

2 The LHCb Experiment

The LHCb experiment is one of the four experiments at CERN's Large Hadron Collider, situated near Geneva, Switzerland. Inside the LHC's 27km long tunnel two opposing proton beams are accelerated until they nearly reach the speed of light and are then brought to collision at the four experiments. These are:

- ALICE (A Large Ion Collider Experiment)
- ATLAS (A Toroidal LHC Apparatus)
- CMS (Compact Muon Solenoid)
- LHCb (LHC beauty)

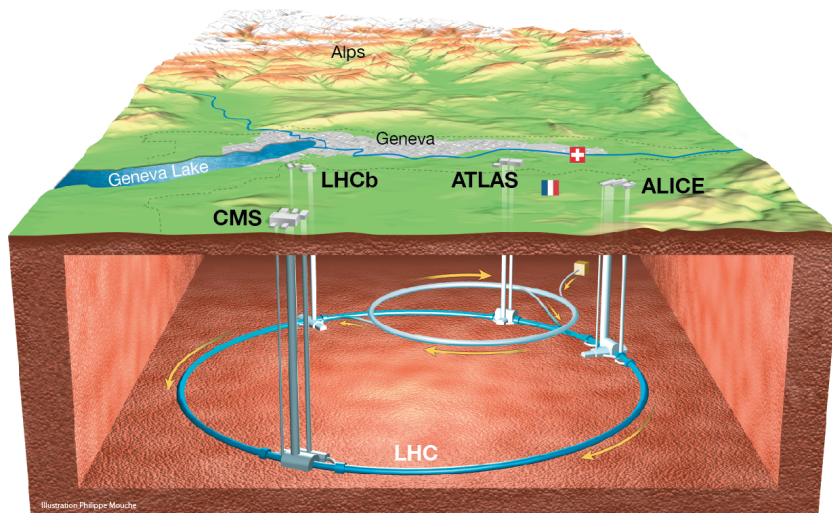


Figure 2.1: Overview of the LHC accelerator ring, the four main experiments and the SPS pre-accelerator. [1]

The ATLAS and CMS experiments are designed as multipurpose detectors and are, therefore, able to investigate a multitude of phenomena like the Higgs boson, extra dimensions, or dark matter particles. The ALICE and LHCb detectors on the other hand are more specialized. ALICE is studying the physics of strongly interacting matter at extreme densities, where the so called quark-gluon plasma forms. The LHCb experiment is testing the Standard Model and also searching for new physics phenomena in decays of B mesons.

2.1 The LHCb Detector

The LHCb detector differs strongly from the other three LHC detectors because it is constructed as single arm forward spectrometer. This design is due to the fact that the particles of interest, B mesons, are mainly produced in the forward direction close to the beam axis. The detector consists of several subsystems which will be briefly described in the following and can be seen in Figure 2.2. All information was taken from [2].

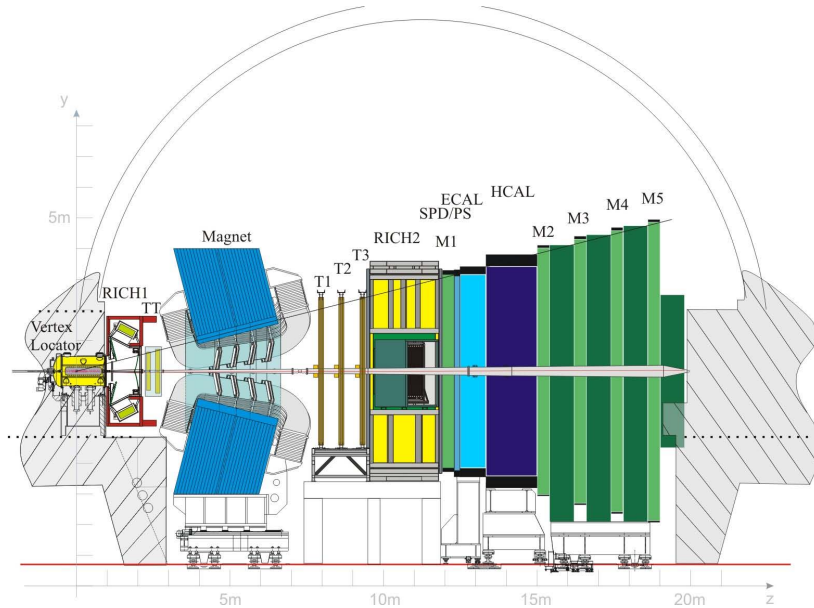


Figure 2.2: Cut through the y - z -plane of the LHCb detector in its current form. [3]

2.1.1 Vertex Locator

The Vertex Locator (VELO) is the first of LHCb's subdetectors and is positioned around the collision point. The primary vertices, where the protons collide, and the secondary vertices, where unstable particles further decay, are reconstructed with a resolution in the x - and y -direction of $10\mu\text{m}$, each.

2.1.2 Magnet

Inside the magnet charged particles are deflected. By measuring their trajectory before and after the magnet the bending and, therefore, the particle momentum can be measured.

2.1.3 RICH Detectors

Two Ring Imaging Cherenkov detectors (RICH) are placed before and after the magnet and are used for particle identification. Charged particles traveling through a medium emit Cherenkov light under an angle θ if their velocity is greater than the speed of light given by $c' = c/n$, where n is the refractive index of the medium. The angle can be expressed as $\theta = \frac{c}{vn}$. By combining the measurement of the angle with the momentum information gained from the tracking system the mass can be estimated, which is then used to identify the particle type.

2.1.4 Tracking System

The LHCb tracking system consists of four stations, the first one the Trigger Tracker (TT) is placed before the magnet and the other three (T1-T3) are placed right after it. Each plane of T1-T3 uses two detector technologies, the Inner Tracker located close to the beam pipe and the Outer Tracker which covers the rest. For the TT and the Inner Tracker, where the particle density is high, silicon micro strip detectors with a resolution of $50\mu\text{m}$ are used. The Outer Tracker uses straw-tube drift chambers with a resolution of $200\mu\text{m}$.

2.1.5 Calorimeters

The calorimetry system is used to identify photons, electrons, and hadrons, and to measure their energy and position. It is divided into four subdetectors. The Scintillating Pad Detector (SPD) determines whether a particle is charged or neutral. The Pre-Shower Detector (PS) sits behind a 12mm thick lead plate where electrons and photons produce electromagnetic showers. Since this happens to less extent for hadrons the PS is used to distinguish between hadrons and electrons and photons. The Electromagnetic Calorimeter (ECAL) consists of alternating layers of scintillators and lead and measures the energy of electrons and photons. The Hadronic Calorimeter (HCAL) is similar to the ECAL but instead of lead iron is used to induce the particle showers.

2.1.6 Muon System

The muon system is composed of five stations (M1-M5) of alternating layers of scintillators and 80cm thick iron plates. It is used to reconstruct and identify muons which is crucial since they are present in many B decays.

2.2 The LHCb Upgrade

After the LHC's long shut-down in 2018, the luminosity at the LHCb detector will increase to $\mathcal{L} = 2 \cdot 10^{33} \text{cm}^{-2} \text{s}^{-1}$ which is five times the current luminosity. This will be achieved by a bunch spacing of 25ns resulting in a readout rate of 40MHz. The current trigger is composed of two levels, named L0 and High Level Trigger (HLT). The readout rate is limited to 1MHz by the L0 level which will be replaced by a software trigger to run at full 40MHz. Along with the trigger, the readout electronics of all subdetectors, but the muon system, have to be replaced to handle the higher occupancy. Especially the performance of the Outer Tracker would decrease dramatically in the new conditions. Therefore it is planned to replace the Inner and Outer Tracker with a new detector, the Scintillating Fibre Tracker (SciFi), which will be described in detail in the following section [4]. See figure 2.3 for the upgraded LHCb detector.

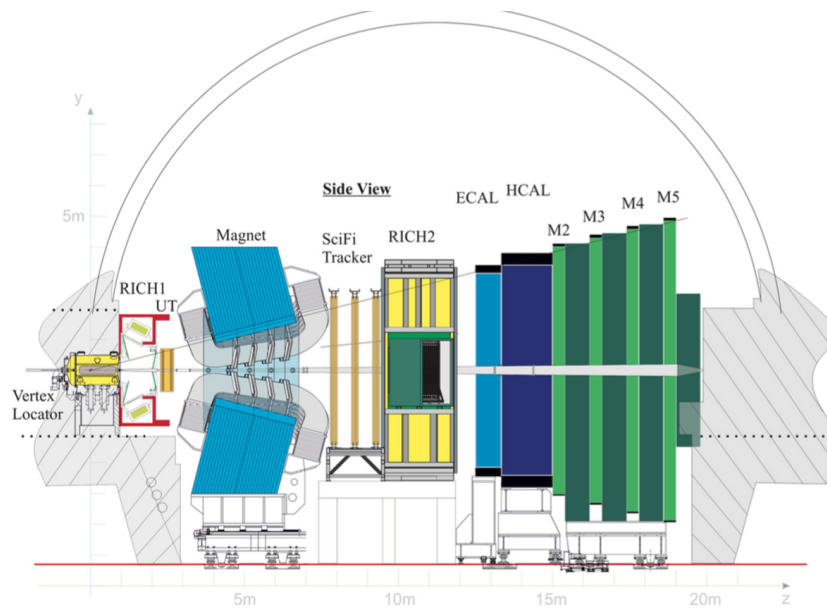


Figure 2.3: Side view of the upgraded LHCb detector. The SciFi Tracker is located between the magnet and RICH. Also TT is replaced by the new Upstream Tracker (UT) and SPD, PS and M1 are removed. [4]

3 The Scintillating Fibre Tracker

The Scintillating Fibre Tracker will replace the current IT and OT of stations T1-T3. It is comprised of three stations each containing four layers, with a size of $6\text{m} \times 5\text{m}$. The second and third layers, so called u and v layers, are rotated around the z-axis by $+5^\circ$ and -5° . The individual layers contain twelve modules with a size of $52\text{cm} \times 5\text{m}$. Each module is then made up of eight fibre mats which are 13cm wide and 2.5m long and supported by a honeycomb and carbon structure. The mats are made of six layers of scintillating fibres with a diameter of $250\mu\text{m}$. Mirrors are glued to the ends of the fibre mats, which are in the center of the module, to increase the light yield. A cross-sectional cut through the module can be seen in Figure 3.2. In total the 144 modules will cover an active region of 360m^2 . Each of the fibre mats will be readout by four silicon photomultipliers (SiPM) which in turn will be readout by the custom designed PACIFIC chip [5].

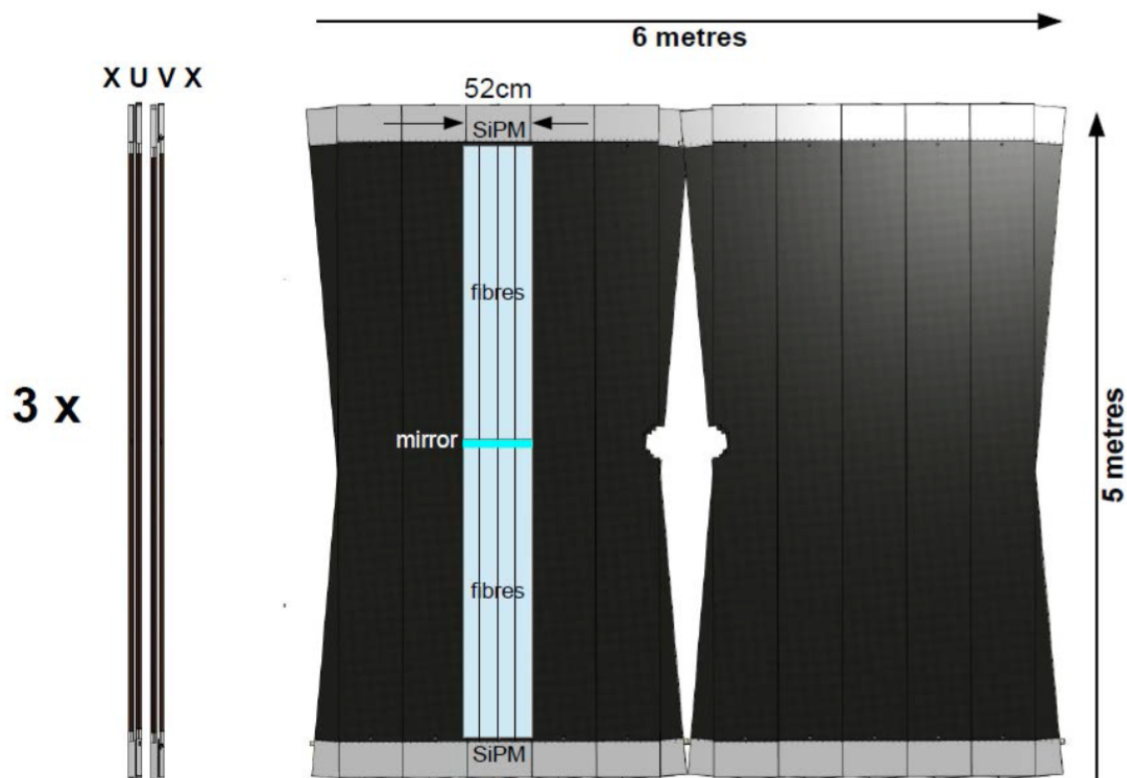


Figure 3.1: Schematic of the SciFi Tracker in the yz- and xy-plane. Highlighted in blue are the eight fibre mats with the mirror in the middle. [5]

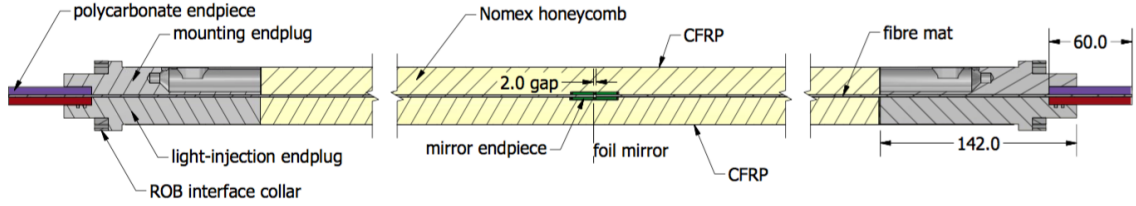


Figure 3.2: Cross-section of a fibre module showing the fibre mat sandwiched between the honeycomb and carbon (CFRP) layers. Also shown are the end pieces to which the readout boxes (ROB) are attached. [5]

3.1 Scintillating Fibres

The scintillating fibres are the active component of the SciFi Tracker. They have a diameter of 250 μ m and consist of three layers, the core, and two claddings. When an ionizing particle passes through the fibre light is emitted through a multi-step process in the core which is then propagated along the fibre fibre through total reflection. By using two claddings with decreasing indices of refraction the angle of total reflection is increased from 21.4° to 27.4° which in turn increases the trapping efficiency from 3.5% to 5.35% [4]. See figure 3.3 for a schematic of the fibre.

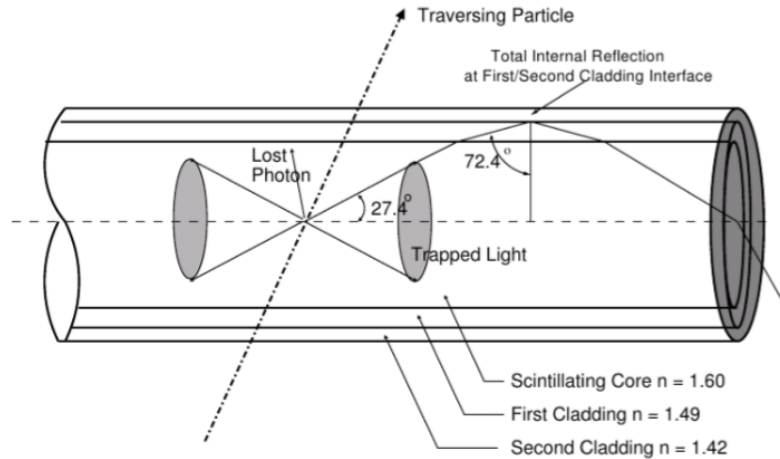


Figure 3.3: Schematic of a scintillating fibre. Light is emitted in the core and then propagated along the fibre through total reflection. [4]

The process responsible for the emission of light is called fluorescence. A particle passing through the fibre will excite the molecule’s valence electron from its singlet ground state S_{00} to an excited state S_{xy} . Here the first index x denotes the electronic states and the second y the vibrational states. The excited electron decays within very short time (<10 ps) to S_{1y} without the emission of radiation through so called internal degradation. The decay from S_{1y} to S_{0y} is then emitting a photon and is called fluorescence [6]. It is shown in figure 3.4.

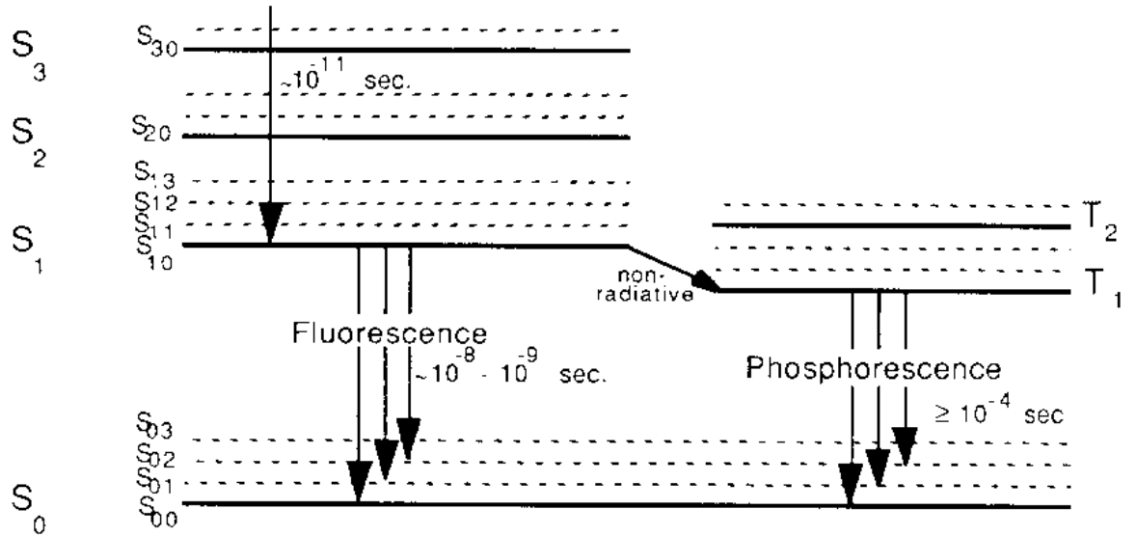


Figure 3.4: Decay scheme for fluorescence and phosphorescence. [6]

The process of phosphorescence is also possible through an intermediate step from the singlet to the triplet state. This only accounts for 10% of the emitted photons and will not be further discussed.

Since the photon has an energy lower than the difference between the levels S_{10} and S_{00} it can travel through the fibre without causing further excitations. The transparency of the fibres is quantified by the attenuation length Λ . It is defined as the length where the initial intensity drops to $1/e$. The intensity at a distance x from the excitation is given by:

$$I(x) = I_0 \cdot e^{x/\Lambda}$$

3.2 Fibre Mats and Modules

The fibres described in the previous section are arranged with high precision into multi-layer fibre mats. To achieve the desired light yield, six layers of fibres are used. The mats are produced by winding the fibre on a threaded turning wheel with a diameter of 0.82m. The thread makes sure the first layer of fibres is aligned precisely with a pitch of 0.275mm. Each following layer uses the fibres below as positioning guide and is therefore shifted by half the pitch. The resulting fibre matrix can be seen in figure 3.5. During the winding process epoxy is applied to hold the fibres together. After taking the mat off the wheel it is still very fragile and thus cast in glue to create a thin protection layer and a precise flat surface. The mat is then cut into the right dimensions and a mirror foil is glued to one end [5].

The winding wheel, in addition to the threads used to align the fibres, also features 2mm deep grooves along its central line. The grooves are filled with epoxy before winding the first fibre layer. They form the alignment pins on the back of the fibre mat which are used to ensure precise positioning during assembly of the modules [5].

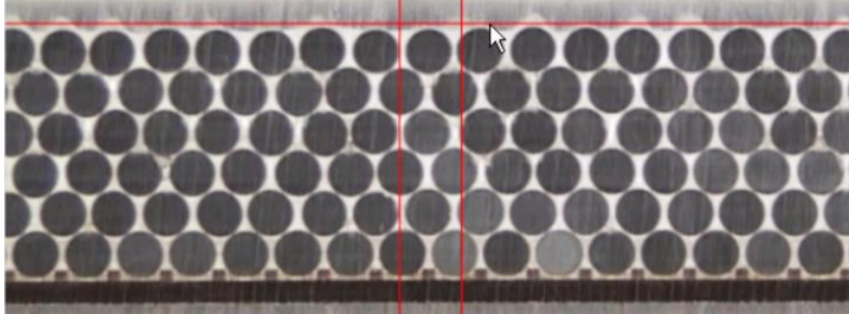


Figure 3.5: View of a fibre mat cast in glue for protection. The fibres measure $250\mu\text{m}$ in diameter and the distance between their cores is $275\mu\text{m}$. The mat is 1.35mm thick. [7]

A fibre module as shown in Figure 3.2 is the assembly of eight mats into a rigid structure which can be mounted onto frames within the LHCb detector and has all the necessary interfaces for the SiPMs and electronics. To produce a module the mats are aligned on a aluminum template which features grooves for the aforementioned alignment pins. Then half-panels of honeycomb laminated with a carbon fibre skin are glued on top of the mats [5].

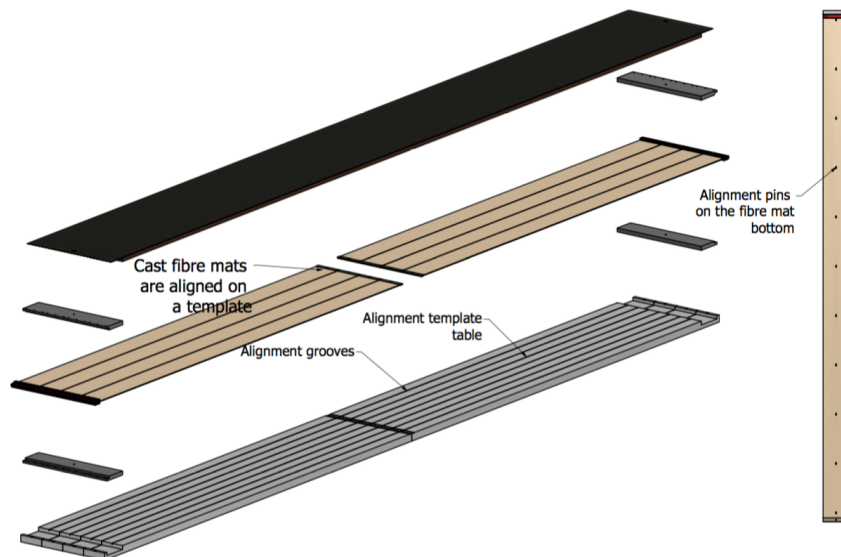


Figure 3.6: Exploded view of the first half of the module assembly. The alignment pins which fit into the grooves of the template are also shown. [5]

3.3 Silicon Photomultipliers

The light emitted by the scintillating fibres is readout by silicon photomultipliers (SiPM) sitting at one end of the mats. The SiPMs are supplied by Hamamatsu and consist of 128 channels arranged into dies of 64, where each channel measures 4×24 pixels. The pixels themselves measure $62.5\mu\text{m} \times 57.5\mu\text{m}$ resulting in a channel size of $250\mu\text{m} \times 1620\mu\text{m}$. See figure 3.7 for a detailed view of a SiPM array.

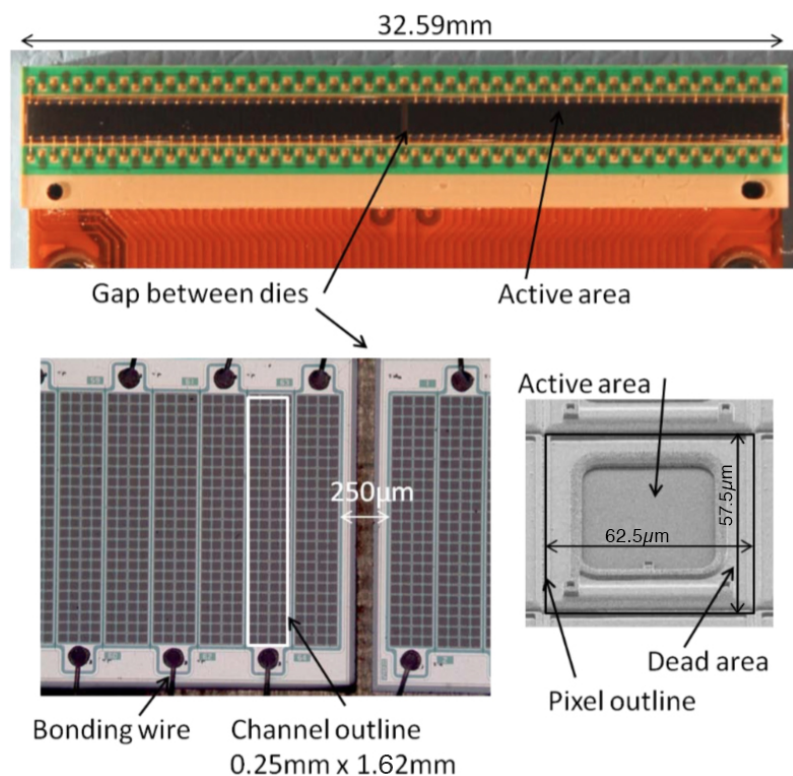


Figure 3.7: Detail view of SiPM structure. Top: Full array consisting of two dies with 64 channels each. Two alignment holes to ensure precise mounting. Bottom left: The channels are shown under the microscope. One can clearly see the the pixels which make up each channel. Bottom right: Detail of a single pixel. [4](edited)

3.3.1 Introduction to Semiconductivity

Solid materials can be found as crystals which are described by solid-state physics as a three dimensional lattice. The atoms inside a crystal are packed so tightly that their energy levels nearly overlap, creating so called energy bands which are separated by band gaps. The difference in electrical conductivity arises from the energy gap between the conduction band and the valence band as well as the Fermi energy.

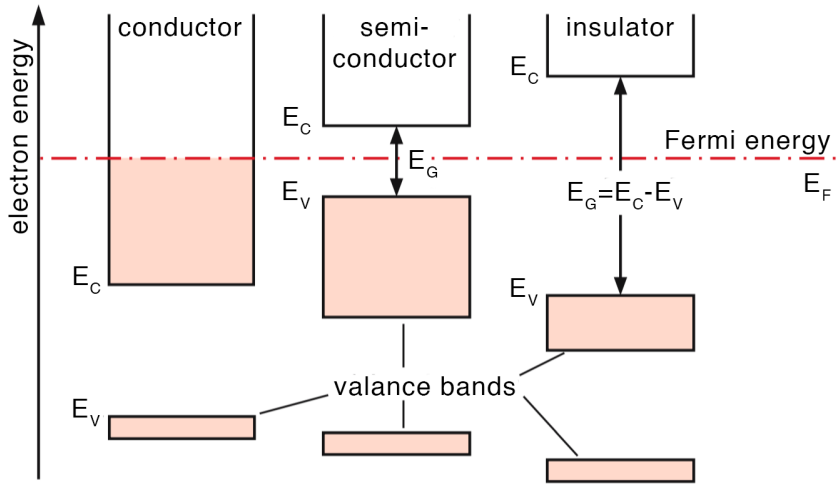


Figure 3.8: Schematic of the energy bands of conductors, semiconductors and insulators. [8](edited)

The Fermi energy (E_F) is defined as the energy up to which the energy bands are filled at a temperature of 0K. The energy gap (E_G) is the difference between the upper boundary of the valence band (E_V) and the lower boundary of the conduction band (E_C), $E_G = E_C - E_V$. Depending on their electrical conductivity the materials can be organized into three categories: insulators, semiconductors and conductors. They are shown in Figure 3.8 and described below:

- **Insulator**

The energy gap of an insulator is in the order of a few eV and thus the probability for a valence electron to move into the conduction band is strongly suppressed. This means there is no electrical conductivity. The Fermi energy is in between the valence and the conduction band.

- **Semiconductors**

Semiconductors have a band gap of around 1eV and a Fermi energy between the valence and conduction band. The gap is small enough to allow electrons from the fully populated valence band to tunnel into the conduction band upon thermal or optical excitation.

- **Conductors**

A conductor either has energy bands that overlap or a partially populated conduction band. In both cases this allows electrons to move into higher energy levels with minimal energy input.

Intrinsic Semiconductors

At temperatures above 0K electrons from the valence band have a chance to tunnel into the conduction band. This leaves a "hole" in the valence band. The electrons

in the conduction band and the holes in the valence band both contribute to the electrical conduction of the semiconductor. For intrinsic semiconductors their densities are equal and denoted with n for negative and p for positive charge carriers. Typical intrinsic semiconductors are silicon (Si) and germanium (Ge).

Doped Semiconductors

Doped or extrinsic semiconductors introduce impurities into the pure crystal such that the charge carrier densities are no longer equal. Depending on the material that is added, the so called dopant, one can distinguish between two types of doped semiconductors:

- **n-type**

The dopant has more electrons in its outer shell than the intrinsic semiconductor, usually phosphor (Ph) or arsenic (Ar). Since the dopant introduces more electrons it is called electron donor.

- **p-type**

Semiconductors of this type are doped with so called acceptors which have a lower number of electrons in their outer shells. Typical elements are aluminum (Al), indium (In), or gallium (Ga).

The dopants are chosen such that their energy levels are near the corresponding energy bands of the intrinsic semiconductor. Donors have to have energy levels close to the conduction band, and acceptors close to the valance band. The doping changes the number of both types of charge carriers which changes the Fermi energy. This is illustrated in Figure 3.9.

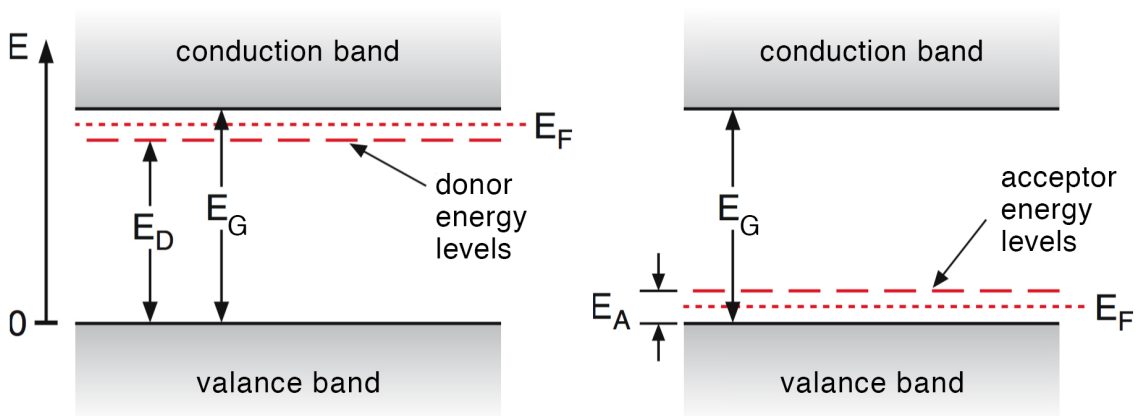


Figure 3.9: Energy levels of a n-type and p-type semiconductor on the left and right side, respectively. [8](edited)

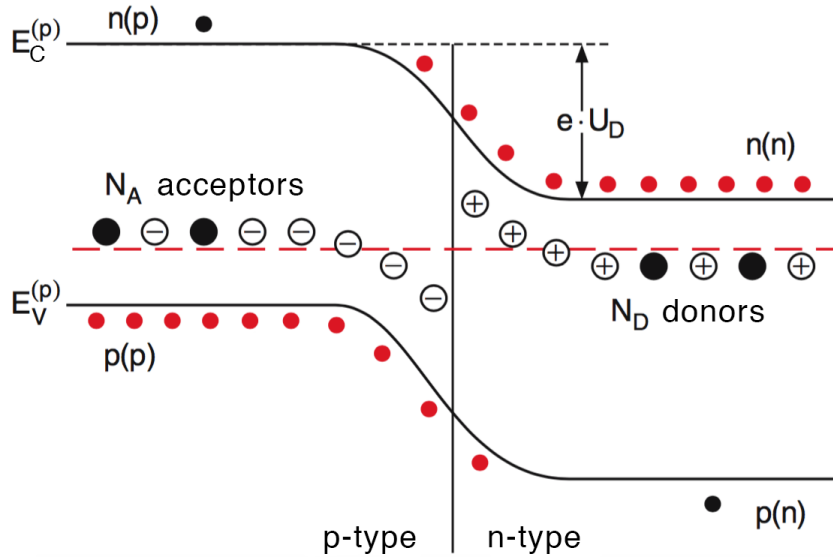


Figure 3.10: Energy bands and charge carrier occupation at the p-n-junction. [8](edited)

3.3.2 p-n-Junction

A p-n-junction is created when a p-type and an n-type semiconductor are brought in contact with each other. In the p-doped region the holes are the dominant charge carriers and the Fermi energy is near the valance band. Whereas in the n-doped region electrons make up the majority of charge carriers and the Fermi energy is near the conduction band. The strong gradient in the concentration of electrons and holes at the junction creates a diffusion current. Electrons move into to the p-type region where they recombine with holes or are captured by acceptors. The holes move in the opposite direction and recombine with electrons or are captured by donators. This process creates a region without free charge carriers around the boundary layer, called depletion region, and an electric field. The electric field results in a drift current in the opposite direction of the diffusion current. Equilibrium is achieved when the sum of both currents is zero. The remaining electric field creates a potential U_D with

$$eU_D = \Delta E_{pot} = E_C^{(p)} - E_C^{(n)} = E_V^{(p)} - E_V^{(n)}$$

This potential bends the boundaries of the valance and conduction as can be seen in Figure 3.10.

When an external voltage (U_{BIAS}) is applied to the p-n-junction it works as a diode. In one direction its resistance is almost negligible (*forward bias*). Whereas in the opposite direction (*reversed bias*) a current will flow when the external voltage is greater than a specific voltage called breakdown voltage (U_{BD}). The corresponding current-voltage curve can be seen in Figure 3.11. The small leakage current below the breakdown voltage is due to electrons tunneling from the valance to the conduction band.

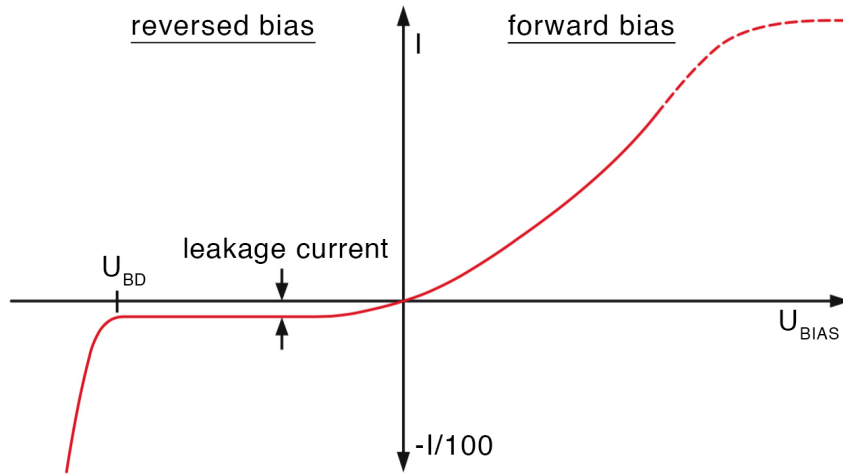


Figure 3.11: Current (I) drawn by the diode as a function of the applied bias voltage (U_{BIAS}) for both modes of operation. [8](edited)

3.3.3 Working Principle of SiPMs

Each of the SiPM's pixel is a so called avalanche photodiode which uses a combination of intrinsic and doped semiconductors. The typical doping scheme ($p^+ - i - p - n^+$) can be seen in Figure 3.12. Incident photons deposit their energy and create electron-hole pairs in the intrinsic area (p^-). When a reversed bias voltage is applied the electrons drift to the multiplication area created by the $p - n^+$ junction. The high electric field in this area accelerates the electrons such that they create further electron-hole pairs.

Depending on the applied bias voltage the diode can be operated in two modes which are illustrated in Figure 3.13. When the bias voltage is below the breakdown voltage the drawn current is proportional to the intensity of the incident light, therefore this mode is called Linear mode. When the bias voltage is above the breakdown voltage the diode is operated in Geiger mode. In this mode the initial electron-hole pair will create an avalanche of charge carriers. The avalanche is stopped by a quenching resistor in series.

The SiPMS are operated in Geiger mode. In this mode the collected charge per pixel does not depend on the number of initial electron-hole pairs and thus does not depend on the number of photons detected in this pixel. Each SiPM channel is comprised of multiple pixels. Multiple photons hitting the same channel but different pixels can be counted by summing up their output.

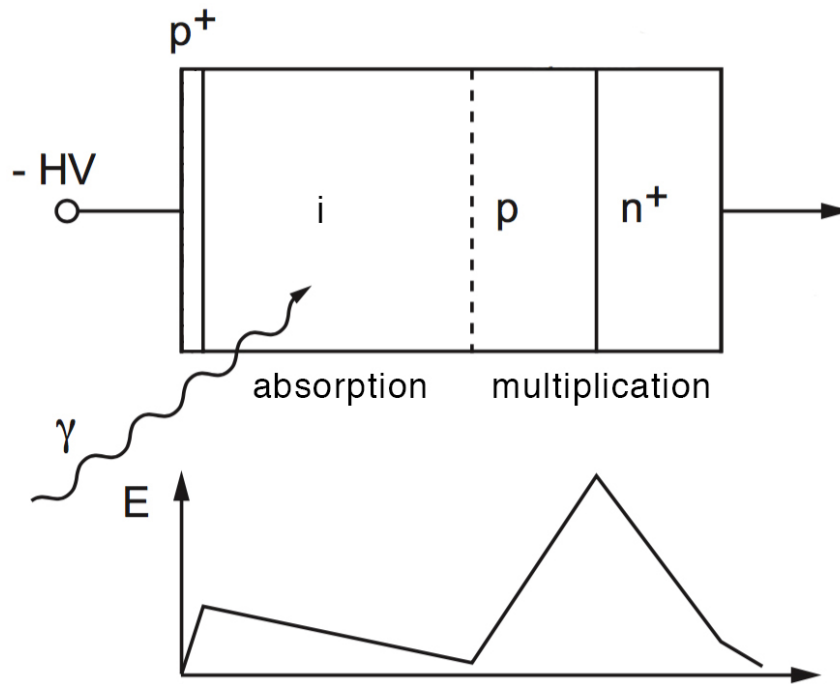


Figure 3.12: Doping scheme and resulting electric field of an avalanche photodiode. The plus indicates highly doped areas and i stands for the intrinsic region. [9](edited)

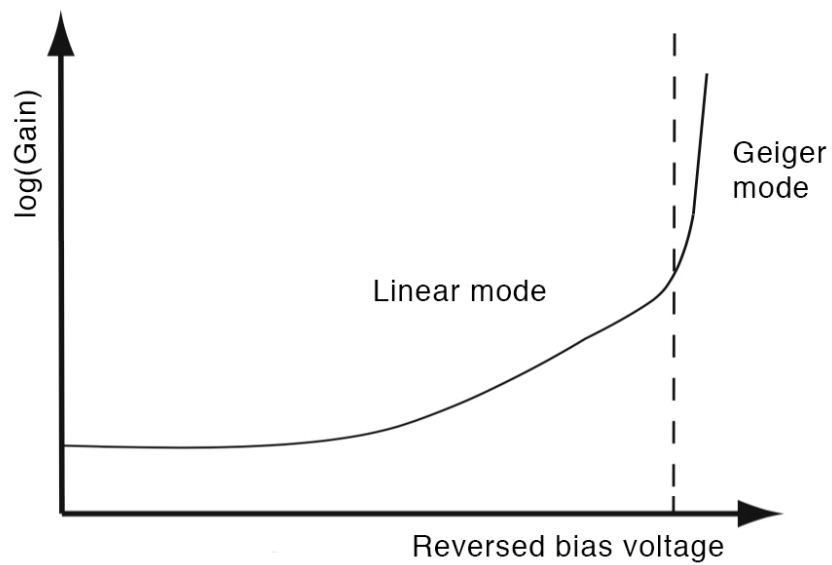


Figure 3.13: Operation modes of an avalanche photodiode. [9](edited)

3.3.4 SiPM Characteristics

In this section the SiPM parameters which are relevant for this thesis are described.

Breakdown voltage

The breakdown voltage is defined as the bias voltage where the electric field of the multiplication area becomes large enough such that each initial electron-hole pair creates an avalanche of electron-hole-pairs. The difference of the bias voltage and the breakdown voltage is called over voltage (U_{OV}):

$$U_{OV} = U_{BIAS} - U_{BD}$$

The breakdown voltage depends linearly on the temperature with a coefficient $\kappa = 53.7\text{mVK}^{-1}$ for the used SiPMs [10].

$$U_{BD}(T) \propto \kappa \cdot T$$

Gain

The gain is the multiplication factor of the elementary charge e inside an avalanche. It depends linearly on the over voltage and the capacity C of the pixel.

$$G = \frac{Q_{avalanche}}{e} = \frac{U_{OV} \cdot C}{e}$$

Each avalanche creates a signal of about the same size. By measuring the difference in collected charge between signals where n pixel fire and where $n + 1$ pixel fire the gain can be determined. See figure 3.14.

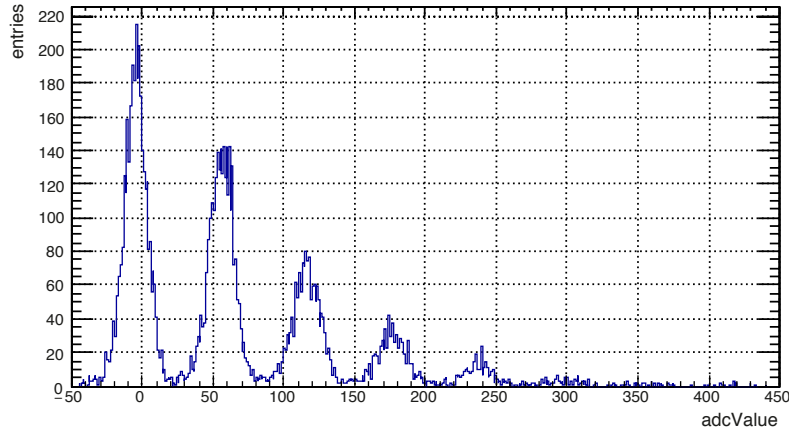


Figure 3.14: Pulse-height spectrum taken with a light source. One can see the equidistant peaks corresponding, from left to right, to 0, 1, 2... photons. The distance between the peaks is the gain in units of ADC.

Photon detection efficiency

The photon detection efficiency (PDE) is the ratio of detected (N_{det}) to incoming photons (N_{inc}). It depends on the quantum efficiency (QE), the Geiger efficiency (ϵ_{Geiger}) and the geometric fill factor (ϵ_G).

$$PDE = \frac{N_{det}}{N_{inc}} = QE \cdot \epsilon_{Geiger}(T, V) \cdot \epsilon_G$$

The quantum efficiency is the probability that an incident photon creates an electron-hole-pair. The probability of that pair to trigger an avalanche is described by the Geiger efficiency and depends on the temperature and the applied voltage. The geometric fill factor describes the fact that not the whole area of each pixel is sensitive to light. For the used SiPMs the PDE is around 39% for photons with a wavelength of 500nm [10].

Dark Count Rate

The dark count rate refers to the noise of the SiPM. Even when no light is shining on the detector the pixels can be fired due to thermally generated charge carriers. The first peak of the ADC spectrum in Figure 3.14 is due to this thermal noise and additional noise coming from the electronics. It is referred to as pedestal peak.

3.4 Readout Electronics

In this section the two different readout ASIC chips used for the readout electronic are presented. The SPIROC-A chip is used for the setup studied in this thesis and the PACIFIC chip is the one that will be used in the data taking of the SciFi Tracker in the LHCb upgrade.

SPIROC-A

The SPIROC-A (**Silicon PM Integrated Read Out Chip - Analogue**) is an analogue, 32 channel chip designed to read out SiPMs. Each of the 32 channels features a low power 5V range DAC to adjust the SiPM bias voltage channel by channel.

Each chip consists of a preamplifier, a shaper with adjustable peaking time from 25ns to 175ns, a track-and-hold stage, and a multiplexed output. The track-and-hold signal is controlled by an external signal and tells the chip to store the current signal amplitude in an analog buffer. To make sure the SiPM signal is sampled at the maximum amplitude the track-and-hold signal has to be timed correctly [11]. See figure 3.15 for the corresponding signal curves.

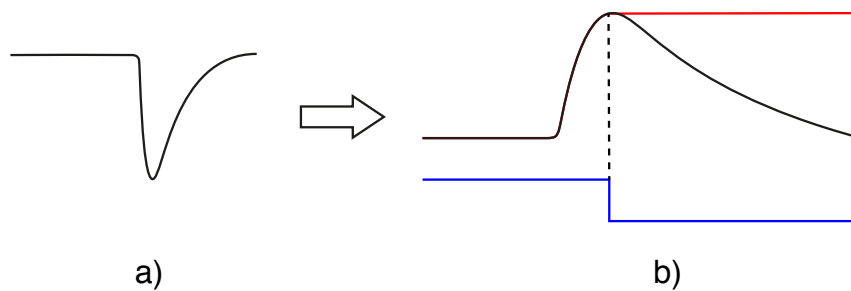


Figure 3.15: Illustration of the signal shaping and track-and-hold method. a) SiPM signal. b) Signal after the shaper (black). When the track-and-hold signal (blue) arrives the current shaper output is stored in the buffer (red).

USBBoard

The USBBoard shown in Figure 3.16 is the DAQ system used to readout and power the front end electronics. The analog SPIROC signals are multiplexed to the USBBoard, digitalized by an ADC, and then saved in the FPGAs FIFO (first in, first out) buffer from where they are transmitted to a PC via an USB interface. The USBBoard is able to readout up to eight uplinks simultaneously. On each uplink one SiPM with its readout card, seen in Figure 3.17, can be attached.

The SPIROC track-and-hold signal can either be triggered internally by the USBBoard or by an external signal.

The USBBoard also features an on board high voltage DC-DC module with a voltage range of 0V to 100V to provide the bias voltage for the SiPMs. The input voltage for the module is controlled by a DAC.

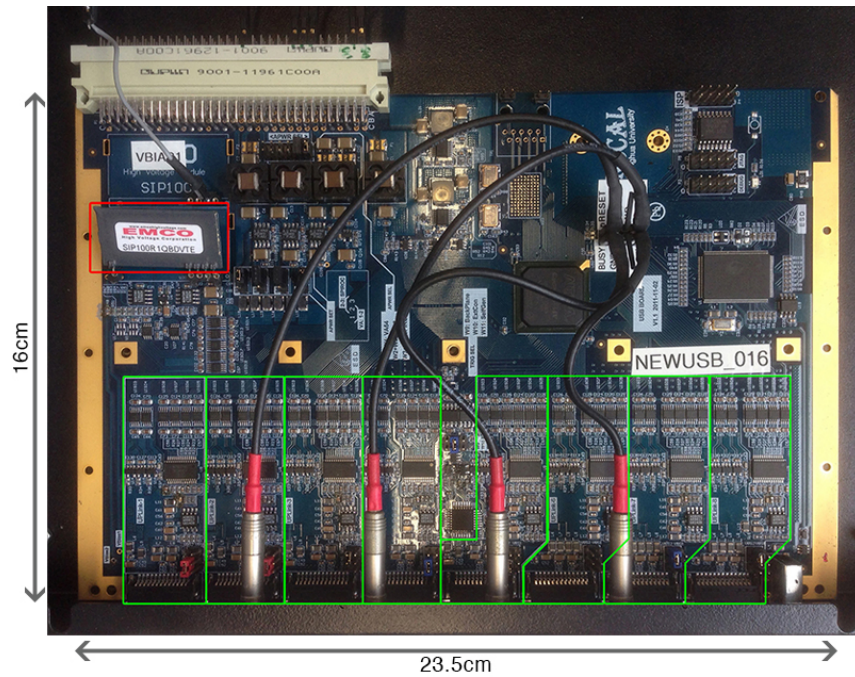


Figure 3.16: USBBoard with the high voltage DAC (red) and the eight uplinks (green) at the bottom. On each uplink one SiPM with it's readout card can be attached.

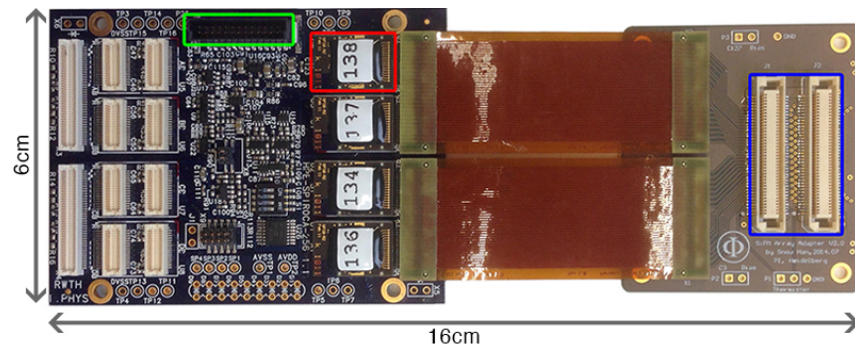


Figure 3.17: Readout card for one SiPM. Blue: SiPM Connector. Red: SPIROC chip. For each SiPM four chips are needed to read out all 128 channels. Green: Connector to USBBoard.

PACIFIC

In the final experiment the SiPMs will be readout by the custom designed PACIFIC (a low Power ASIC for the sCIntillating FIBres traCker) chip. In contrast to SPIROC-A it will read out all 128 SiPM channels and digitalize their signal on chip with a rate of 40MHz. The signal chain can be seen in figure 3.18.

The current coming from the SiPM is first processed by a preamplifier and converted into a voltage which is then shaped inside the fast shaper such that 90% of the signal is accumulated within the first 10ns. The signal then gets integrated and digitized using three comparators with tunable thresholds [4].

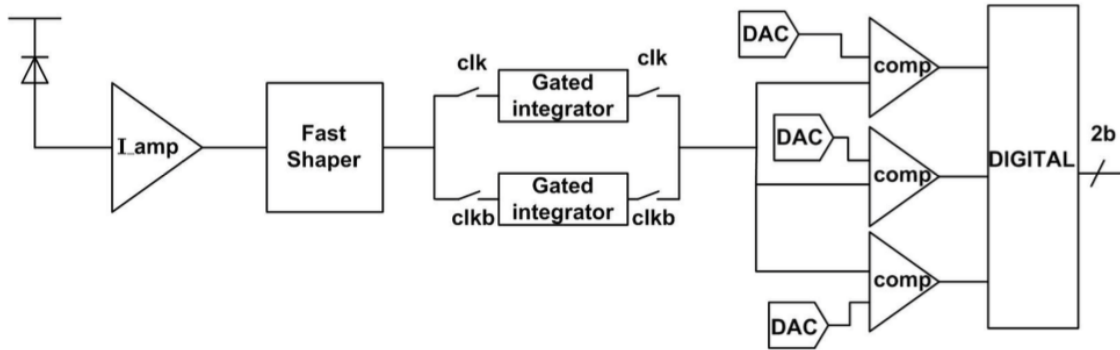


Figure 3.18: Schematic of the different stages for the readout of one channel of the PACIFIC ASIC which consists of a preamplifier, fast shaper, two integrators, and three comparators. [4]

4 Experiment Setup

The experiment setup studied in this thesis consists of the following components:

- **Fibre Module**

In this thesis the properties of two fibre modules are studied. The modules are comprised of one fibre mat and are 1m and 2.5m long, respectively.

- **Trigger Setup**

Two scintillation counters which are connected to form a coincidence are used to trigger on cosmic rays passing through the module. The trigger is described in detail in Chapter 7.

- **Front end electronics**

The front end electronics consist of four SiPMs and their readout cards to readout the full width of the module. They are installed inside a readout box which is mounted to the module. See Figure 4.1b.

- **Back end electronics**

One USBBoard is used to readout and power the front end electronics.

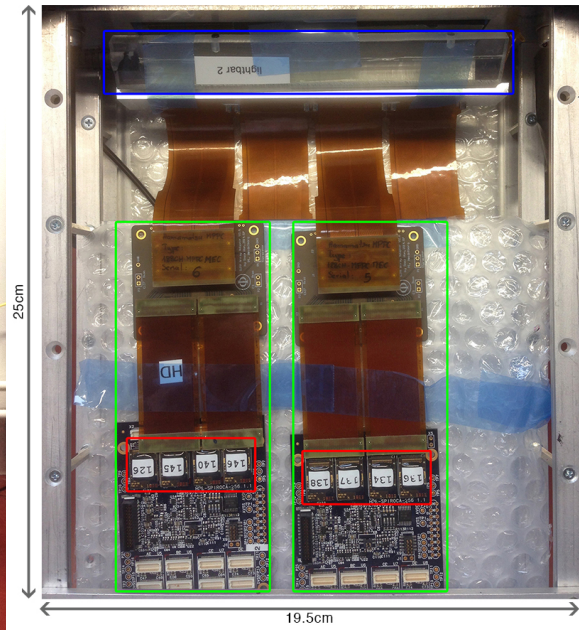
- **Light Injection System**

The light injection system is used to calibrate the SiPMs. The light from an LED is transmitted through an optical fibre to a so called lightbar which is mounted to the module near the SiPMs. The LED is driven by a function generator.

The whole setup is mounted on a supporting rack and can be seen in Figure 4.1a.



(a)



(b)

Figure 4.1: a) The experiment setup mounted on the black supporting rack. The components are from top to bottom: readout electronics, scintillation counters, fibre module, NIM crate with trigger electronics.

b) View into to the readout box which contains the front end electronics consisting of four SiPMs and their readout cards (green). Each card is equipped with four SPIROC chips (red). The lightbar (blue) used to inject light into the fibre mat is attached above the SiPMs.

4.1 Calibration of the DAC Controlled DC-DC Converter

The DAC controlling the DC-DC module needs to be calibrated in order to know which DAC value corresponds to which output voltage of the module. For this the DAC range is scanned in steps of 500 and at each point the output voltage is measured with a multimeter.

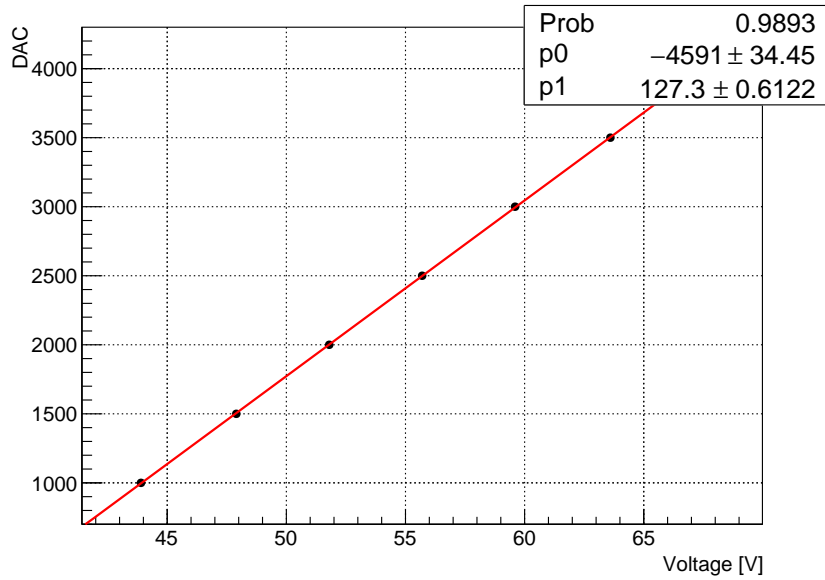


Figure 4.2: DAC value and corresponding measured voltage. A linear fit is used to determine the calibration parameters p_0 and p_1 . The error on the individual voltage measurements is 0.1V. It is not visible in this plot.

The DAC value corresponding to a voltage U can now be calculated according to:

$$DAC(U) = 127.3[V^{-1}] \cdot U[V] - 4591$$

4.2 Delay Time Scan

As described in section 3.4 a correct time adjustment of the track-and-hold signal is crucial when using the SPIROC ASIC to read out SiPMs. To ensure the signal is sampled at the maximum amplitude the delay time of the track-and-hold signal has to be adjusted. This is done by a delay time scan using the light injection system. The delay time is set in steps of 25ns clock cycles and for each time the mean amplitude of 10,000 signals is recorded. Figure 4.3 shows the strong dependence of the mean amplitude on the delay time. The best timing for the light injection system is achieved using a delay time of 36 clock cycles (900ns).

The time between an LED pulse being generated and the corresponding electrical signal in the SPIROC ASIC peaking is measured to be about 200ns. This value is later used as the delay time of the cosmic particle trigger. An illustration of the signal chains when using the light injection system and the particle trigger is shown in Figures 4.4 and 4.5, respectively.

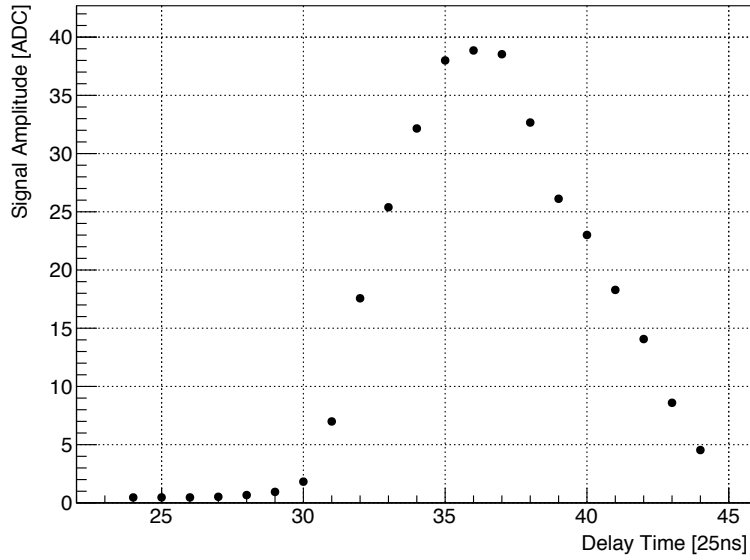


Figure 4.3: Delay time scan in steps of 25ns clock cycles. The highest mean value (38.856) is measured at 36 clock cycles.

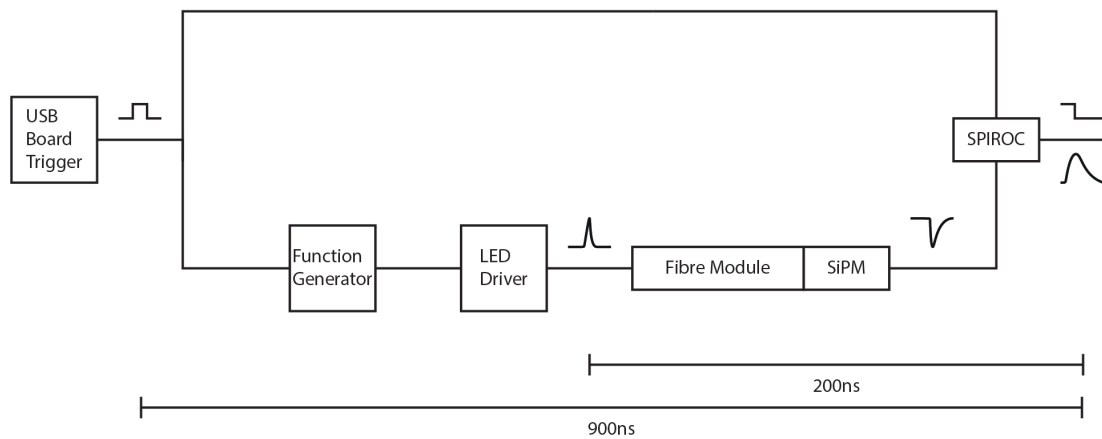


Figure 4.4: Signal chain using the light injection system. The track-and-hold signal has to be delayed by 900ns. The time between an LED pulse being generated and the corresponding SPIROC signal is 200ns.

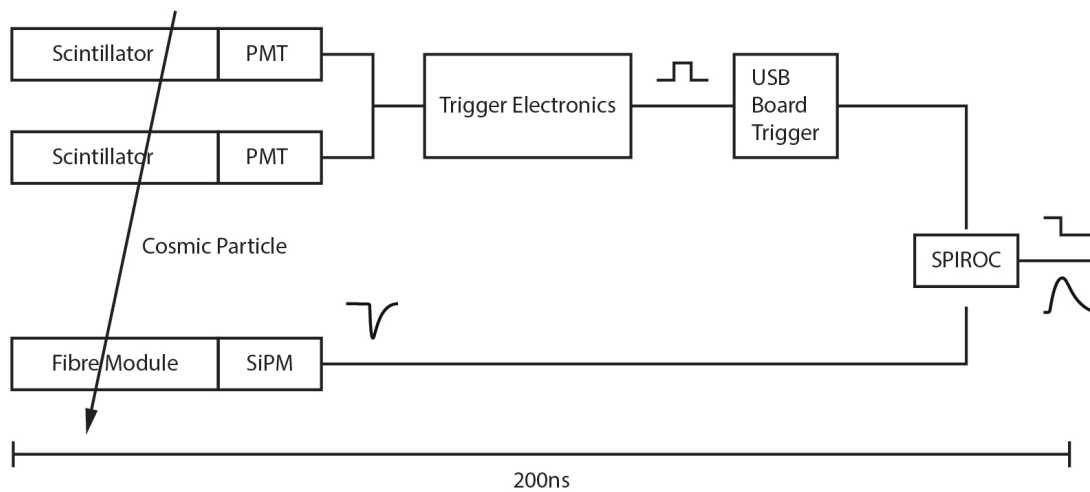


Figure 4.5: Signal chain when taking data with cosmic particles. The trigger signal for the track-and-hold signal is now coming from the trigger setup. This signal has to be delayed by 200ns.

5 SiPM Calibration

The first step of commissioning the cosmic setup is to make sure the readout electronic performs uniformly for all SiPM channels. Therefore this section describes a procedure to calibrate the SiPMs using a light injection system.

Each SiPM channel has an intrinsic breakdown voltage which, for older SiPM models, can vary up to 0.5V from channel to channel. This variation in breakdown voltage means the channels operate at different over voltages and thus have different PDEs. As can be seen in figure 5.1 a difference of 0.5V in breakdown voltage translates to a difference of 2.5% in PDE for 500nm photons.

The SPIROC's feature to tune the voltage applied to each channel is used to compensate for this variation in breakdown voltage.

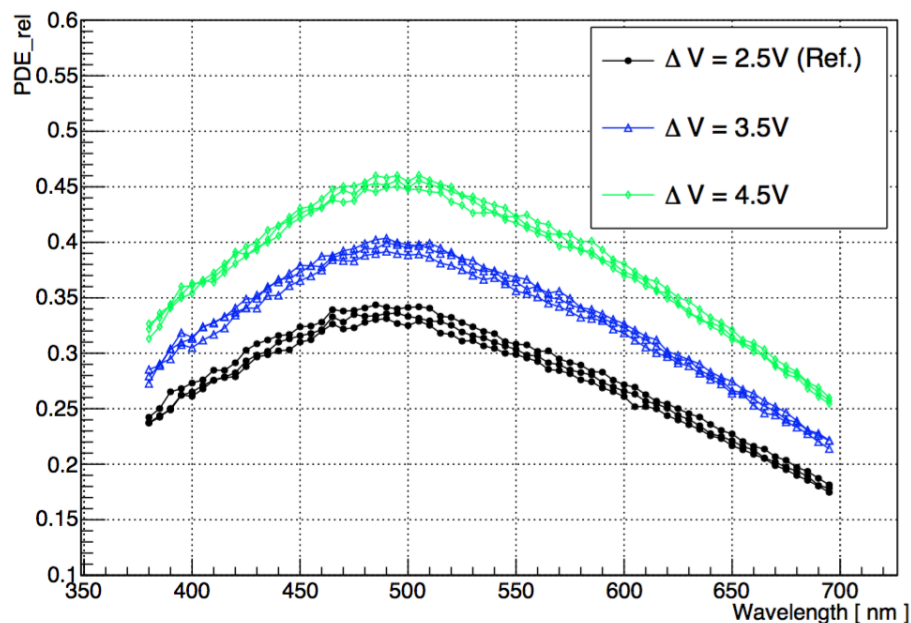


Figure 5.1: Photon detection efficiency (PDE) for different over voltages (ΔV) and wavelengths. [10]

5.1 Calibration Routine

The goal of this calibration is to tune each of the SiPM's channels to run at the same effective breakdown voltage ($\overline{V_{BV}}$). The calibration routine consists of the following steps:

1. Measure the gain of each channel at different V_{BIAS}
2. Extrapolate V_{BV} from the $gain - V_{BIAS}$ curve
3. Calculate and set the SPIROC DAC

Step 1: Gain Measurement

In order to determine the gain of each channel one injects light into the fibre mat using the lightbar and an LED driven by a function generator. This leads to at least one photon to be seen by each channel in each event.

The recorded pulse-height or ADC spectrum has several peaks which correspond to the number of detected photons. Those peaks are then fitted using the sum of several gaussians with the following free parameters: position of the first peak, width of the peaks, and distance between the peaks. The average distance between the gaussians is the gain value. An example of the ADC spectrum and the obtained fit result can be seen in figure 5.2.

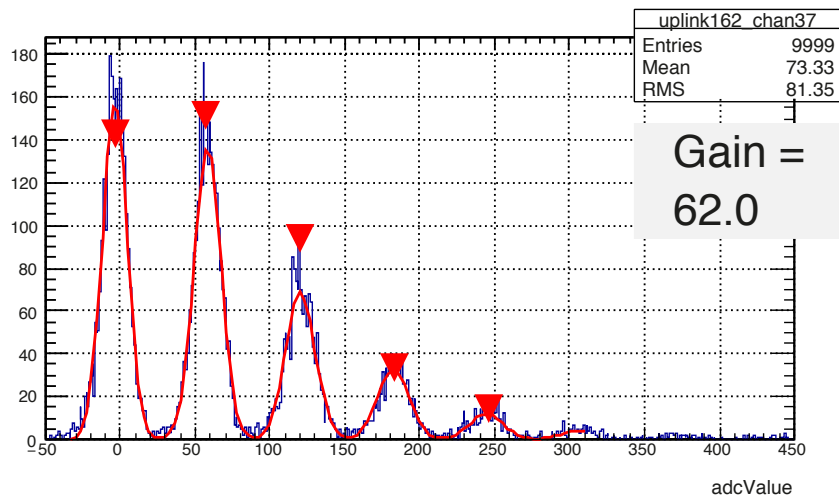


Figure 5.2: ADC spectrum from light injection system and fit result. The gain value is the distance between the peaks. The red triangles indicate the peak position found by the fit software.

Step 2: Breakdown Voltage Extrapolation

To determine the breakdown voltage the gain of each channel is recorded at various bias voltages. The resulting gain-voltage curve is fitted using a linear function. If the gain is plotted on the x-axis and the bias voltage on the y-axis, the breakdown voltage corresponds to the y-intercept of the the linear function. An example of such a plot can be seen in Figure 5.3.

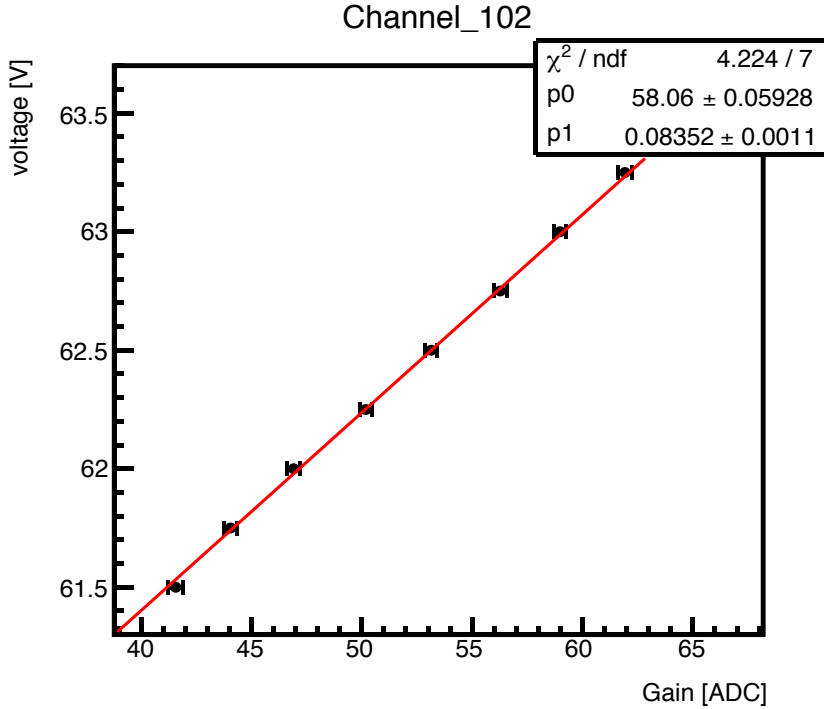


Figure 5.3: Plot and obtained fit result to determine the breakdown voltage for one channel. The breakdown voltage corresponds to the fit parameter p0. The error on the gain is obtained from the error on the gain fit result.

Step 3: Calculating and Setting the SPIROC DAC

The SPIROC's 8 bit DAC, in principle, allows to tune the bias voltage over a range of 4.4V but since it is highly non monotonic (see appendix A.1) only a smaller voltage range can be set predictably. Therefore the initial DAC value was set to 94 which allows to tune the voltage over a range of 1.1V or from 63 to 125 in terms of DAC values which is enough leverage to tune the given SiPMs. Inside this range the voltage can be set in increments of 18mV.

The new DAC value, to tune each individual channel, can be calculated according to:

$$DAC = \frac{\overline{V_{BV}} - V_{BV}}{-0.018} + DAC_{old}$$

Where DAC_{old} is the DAC value set before.

5.2 Calibration Results

Before calibration the breakdown voltage distribution for all 512 channels of the four SiPMs has a spread (RMS) of 360mV and features several peaks. After four calibration runs the distribution looks like a gaussian and has a spread of only 62.5mV which is of the same order of magnitude as the fluctuations caused by temperature changes of 1K.

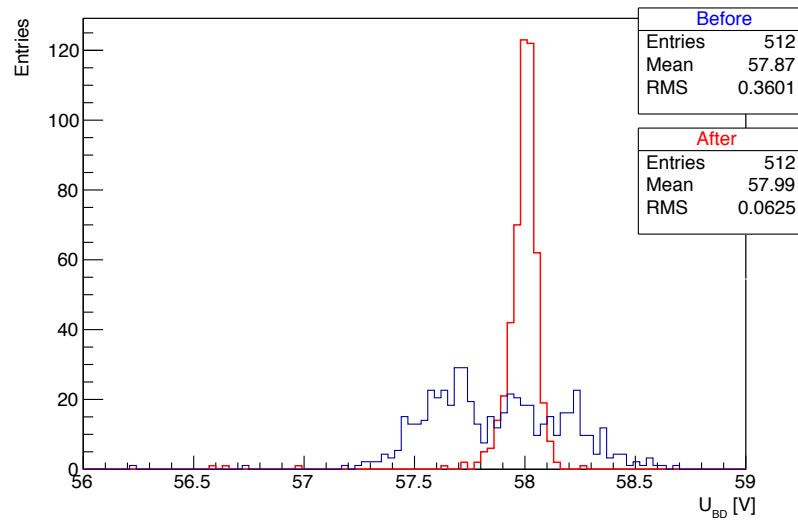


Figure 5.4: The breakdown voltage distribution of all 512 channels. Before calibration the RMS is 0.3601V. After four calibration runs the distribution has an RMS of 0.0625V.

6 Cosmic Rays

Cosmic rays are produced as primary cosmic rays through various astrophysical processes and are mainly composed of protons and α -particles. When those primary particles hit the molecules in the earth's atmosphere they decay in a cascade of neutrons, pions, positrons, and muons, forming the secondary cosmic rays [12]. This process can be seen in Figure 6.2.

6.1 Primary Cosmic Rays

The primary cosmic radiation striking the earth's atmosphere consists of particles which are produced and accelerated in astrophysical processes. It is comprised of 87% protons, 12% α -particles, and 1% heavy ions [12]. In contrast to the composition of the radiation which is well understood, its origins are still up to debate. The two most popular theories for their sources are shockwaves produced by supernovae explosions, and particles accelerated near black holes [12]. But those theories fail to explain particles whose energy exceed 10^{11} GeV.

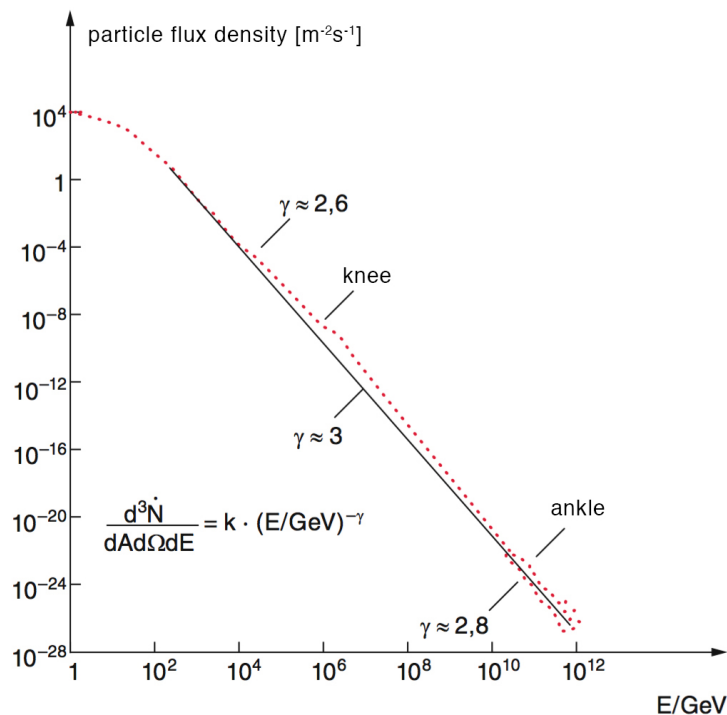


Figure 6.1: Energy spectrum of the primary cosmic radiation. The energy is proportional to $E^{-\gamma}$. [12](edited)

The energy spectrum of the primary cosmic radiation seen in Figure 6.1 extends over 32 orders of magnitude. For energies above 10GeV it follows a power law with varying exponents γ and two abrupt changes called "knee" and "ankle". Up to an energy of 10^6 GeV the index is 2.6, from the knee to the ankle it is 3, and for energies exceeding 10^{10} GeV it is 2.8. In principle one would expect a cut-off of the spectrum at 10^9 GeV called the Greisen-Zatsepin-Kuzmin cut-off (GZK) due to interactions with the cosmic microwave background, but still particles exceeding this energy are observed [13]. It is speculated that they might originate from outside our galaxy.

6.2 Secondary Cosmic Rays

Secondary cosmic radiation is produced when a primary particle collides with a molecule inside the earth's atmosphere, mainly nitrogen and oxygen. This process can be seen in Figure 6.2. The atmosphere has an atmospheric depth of about 1000gcm^{-2} and the interaction length for protons is 90gcm^{-2} in units of area density [9]. This means that only about 0.02% of the primary protons reach the earth's surface. The decay products are mainly charged pions and kaons which then decay through weak interaction producing muons, neutrinos, and, in the case of kaons, also additional pions. The muons have a lifetime of about $2.2\mu\text{s}$ and may decay into electrons and neutrinos before reaching the surface. The cosmic radiation on the earth's surface is mainly composed of muons and neutrinos. Since the scintillating fibres are only sensitive to ionizing radiation only the muons will be discussed further.

Of the charged particles hitting the surface about 80% are muons with a mean energy of 4GeV. The muon flux on the ground depends on the zenith angle θ .

$$I(\theta) = I_0 \cdot \cos(\theta)^k$$

For angles $\theta \neq 0$ it is lower because the muons travel a longer distance inside the atmosphere and are more likely to decay. The exponent k depends on the energy of the muons and is approximately 2 for 3GeV. For higher energies the distribution becomes more flat. The flux of muons at sea level is about $I \approx 1\text{cm}^{-2}\text{min}^{-1}$.

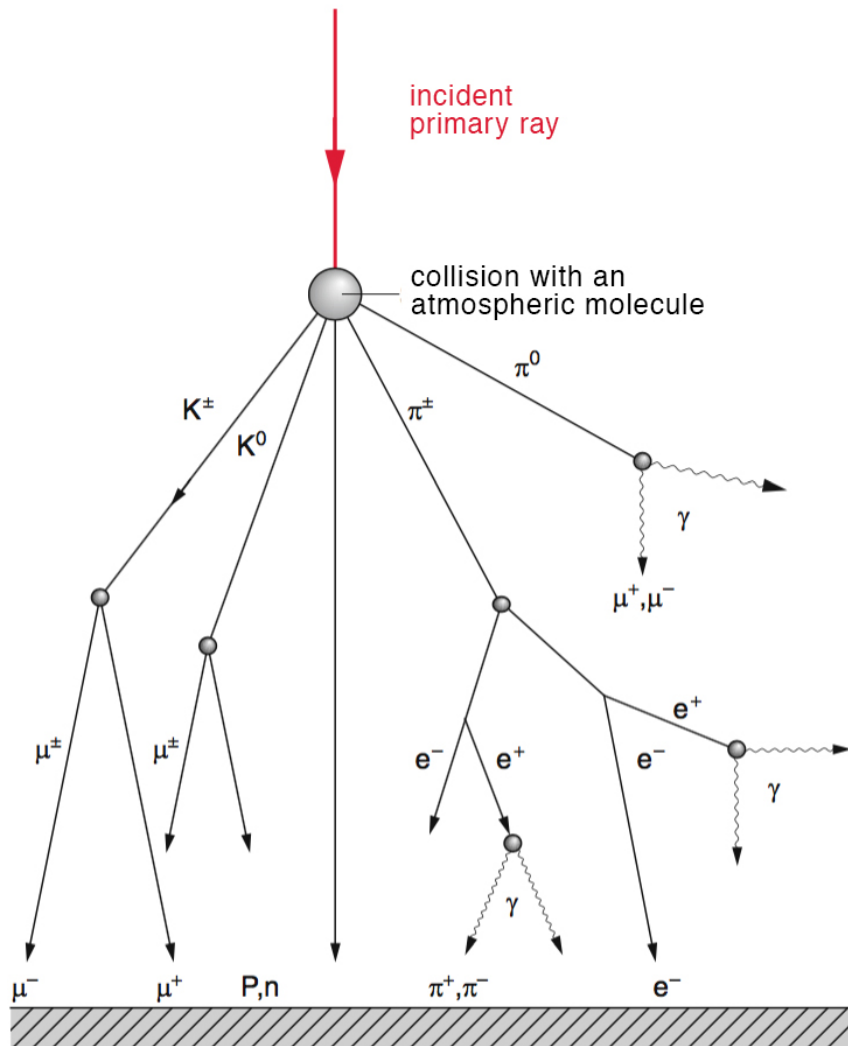


Figure 6.2: A primary cosmic particle collides with an atmospheric molecule and decays in a cascade of secondary particles. The secondary cosmic rays can be detected on the earth's surface. [12](edited)

7 Trigger Setup

A trigger is a system which decides whether an event in a particle detector is recorded or not based on simple criteria. The trigger indicates that a cosmic particle passes through the module and thus allows to distinguish between physically interesting events and noise.

The trigger used in this experiment is shown in figure 7.1 and consists of two scintillation counters positioned above the fibre module. The analog signals coming from the photomultiplier tube (PMT) are fed into discriminators with tunable thresholds to reduce noise. When a PMT signal is above the threshold a fixed width pulse is generated. The AND-logic is used to form a coincidence from both PMT signals. Only when both of them fire inside a time window given by the width of the discriminator signal, a trigger signal is generated.

The trigger signal then tells the USBBoard to read out the fibre module. It is vetoed by the "BUSY" signal sent by the USBBoard to prevent further trigger signals during signal sampling and when the FIFO buffer is full.

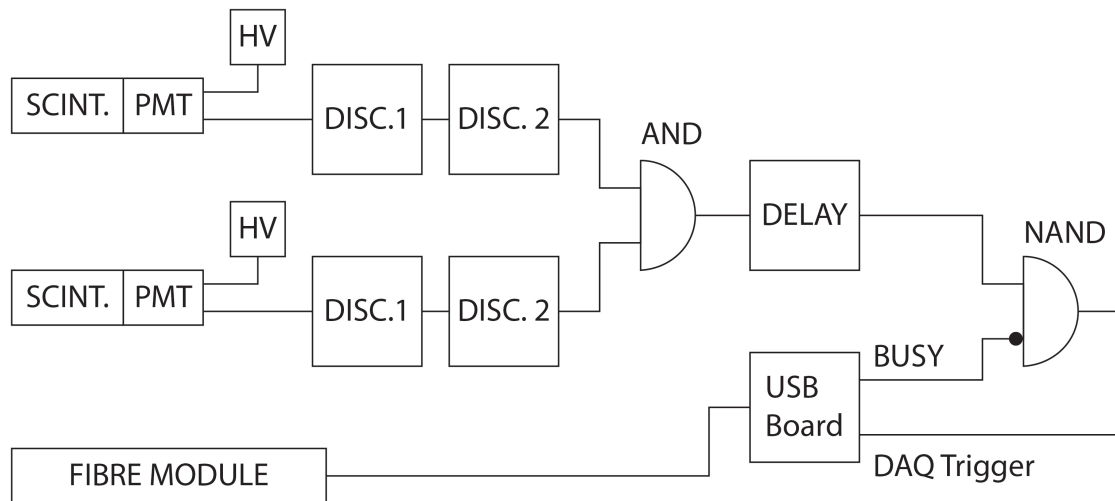


Figure 7.1: Schematic of the trigger setup.

7.1 Scintillation Counters

A scintillation counter is used to detect and measure ionizing radiation. It works by detecting the light emitted in a scintillator upon excitation through the ionizing radiation. A typical counter, as the one used in the experiment, has the following components:

- **Scintillator**

The scintillator converts the incident radiation into light. The atoms of the scintillator are excited when struck by the radiation and upon relaxation emit light of a characteristic wavelength [9]. This process is described in more detail in section 3.1.

- **Light Guide**

The scintillator usually has a different geometry than the PMT. Therefore a light guide made from acrylic glass is needed to transmit the light [9].

- **Photomultiplier tube**

The photomultiplier converts the photons emitted by the scintillator into electrons using a photocathode. Those electrons are then accelerated through a system of dynodes creating an avalanche effect and thus a measurable current [9].

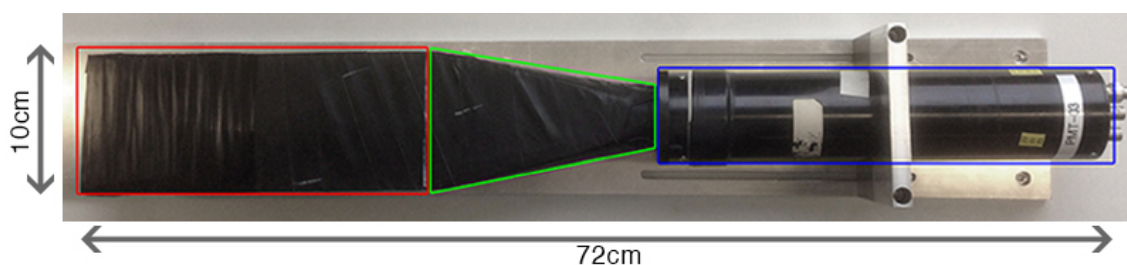


Figure 7.2: One of the two scintillation counters used for the trigger setup. Red: Scintillator. Green: Light Guide. Blue: Photomultiplier tube (PMT).

7.2 Electronics

The electronics used in this setup are so called NIM modules and fit into special power crates. They all conform to the NIM (Nuclear Instrument Module) standard which means that the modules and crates have standardized dimensions and voltages. The voltages provided by the power crate are: $\pm 6V$, $\pm 12V$ and $\pm 24V$. The modules used for the trigger are discriminators, logic units, power supply, scaler, NIM to TTL converter and a delay unit, they can be seen in figure 7.3.



Figure 7.3: Picture of the trigger electronics. From left to right: High voltage power supply, scaler, delay unit, NIM to TTL converter, TTL NAND-logic, AND-logic, discriminator, discriminator.

7.2.1 Discriminators

A discriminator provides a logic signal if the incoming signal exceeds a certain adjustable threshold. This allows to filter out the real signals from any low amplitude noise, and to convert analog signals into digital ones which can be used in logic circuits [9]. The NIM standard uses 0V and -0.8V for logic 0 and 1, respectively. For this setup one discriminator would have been sufficient but the module with the right threshold range (0mV to -50mV) provides logic signals with a varying and too small width which make it impossible to form a coincidence. Therefore the signals coming from the first discriminator are processed in a second discriminator. The second discriminator has the wrong threshold range for the analog PMT signal but provides a nice digital signal with adjustable width.

7.2.2 Logic Units

Logic units are used to combine the digital signals coming from the discriminators or the USBBoard. The coincidence for the trigger signal is made with an AND logic which gives a signal whenever the two input signals (logic 1) overlap in time. The NAND logic used to veto the trigger signal on the other hand only gives a signal when the BUSY signal is 0 and the trigger signal 1.

7.2.3 Delay Unit

Delay units allow to delay signals by an adjustable time. They consist of several cables with different lengths. A signal needs a certain amount of time to propagate through a cable. The total amount of cable the signal has to propagate through

inside the delay unit can be set on the box's face. For the used delay unit the delay time could be adjusted from 0ns to 31.5ns.

7.2.4 Scaler

A scaler counts incoming logic signals and displays the number on the front. It allows in a quick way to verify signal rates from the PMTs or the coincidence.

7.2.5 NIM to TTL Converter

A NIM to TTL converter converts the signal from the NIM to the TTL standard. The NIM standard uses 0V for logic 0 and -0.8V for logic 1 whereas the TTL standard uses 0V and 2V, respectively. The trigger signal coming from the NIM modules has to be converted from NIM to TTL because the USBBoard only responds to TTL signals.

7.3 Adjusting the PMT Voltage

The PMTs can be operated at a wide range of voltages. Usually the manufacturer provides a recommended operational voltage but this might not be the ideal one for each application. To find the exact voltage a plateau measurement for both PMTs is done using the setup shown in figure 7.4.

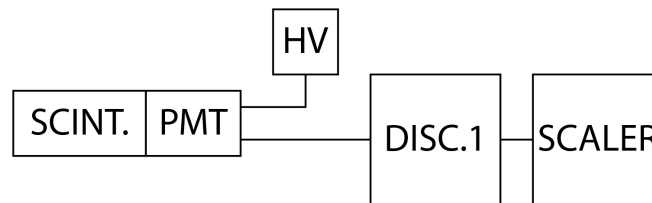
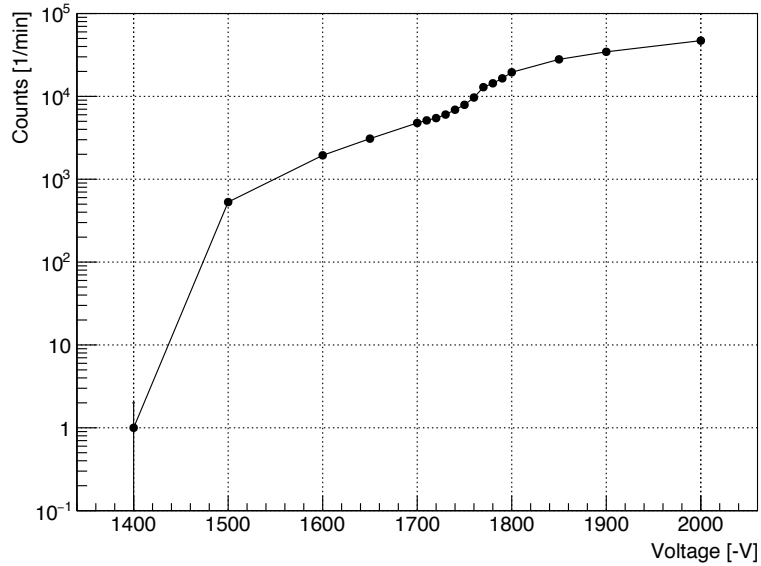


Figure 7.4: Setup for the plateau measurement consisting of the scintillation counter, high voltage power supply, discriminator, and scaler.

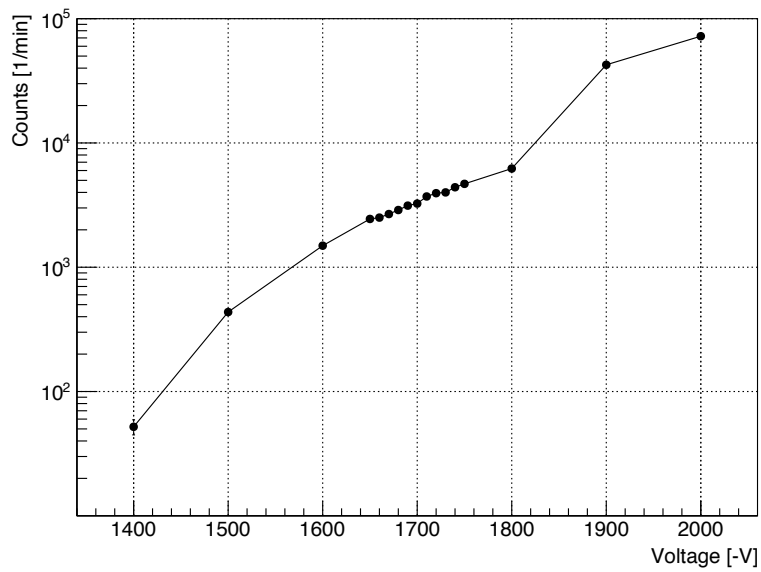
The discriminator analyses the signals coming from the PMT and if they exceed the threshold, a digital signal is send out. This signal then increments the scaler. For each applied voltage the rate is measured over one minute. The threshold is set to -10mV so that nearly all signals pass the discriminator.

The results for both PMTs can be seen in figure 7.5. If the voltage is set too low the signals from the PMT can not pass the discriminator, which for PMT 01 happens below -1400V. At around -1500V the rate increases dramatically and reaches a region with a smaller gradient. All particles now trigger a PMT signal large enough to pass the discriminator and thus the rate depends only little on the applied voltage. After this the rate goes up again because noise is amplified beyond the threshold.

Since both graphs do not have a clear plateau the ideal operational voltage was chosen to be within a region with no jumps in the rate. The chosen voltages are -1710V for PMT 01 and -1660V for PMT 03.



(a) PMT 01



(b) PMT 03

Figure 7.5: Plateau measurement for PMT 01 and PMT 03. The count rate is measured while varying the high voltage to determine the best operational voltage.

7.4 Adjusting the Discriminator Thresholds

The discriminator gives a signal when the incoming signal exceeds the threshold. For both discriminators used in this setup the thresholds can be adjusted via a potentiometer on the face of the module. The threshold can be adjusted from 0mV to -50mV for discriminator 1 and from 0V to -10V for discriminator 2. The thresholds are measured with a multimeter and for discriminator 2 are multiplied by a factor 10, so the actual range is 0V to -1V. Otherwise the logic signals from the first discriminator never would have passed the second one at the chosen thresholds. The setup used to adjust the threshold is nearly the same as in figure 7.4 only now both discriminators are attached before the scaler.

In this section the results for thresholds concerning PMT 01 are presented, the results for PMT 03 can be found in the appendix A.2.

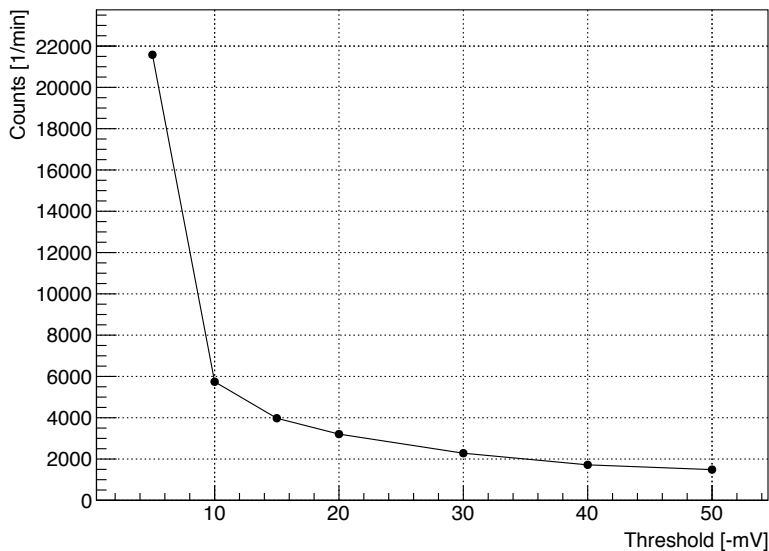


Figure 7.6: Threshold measurement for discriminator 1 of PMT 01. The count rate is measured over one minute at various threshold voltages.

Below a threshold of -10mV noise coming from the PMT is able to trigger a discriminator output. Above -10mV physically relevant signals might be cut off. A threshold of -10mV is chosen for the first discriminator of PMT 01 and PMT 03.

The threshold of the second discriminator has to be set such that it does not introduce any additional noise or cut off relevant signals. Therefore the count rates after the first discriminator (C_1) and after both discriminators (C_2) were measured simultaneously. Ideally the second discriminator would always fire when the first fires and the ratio C_2/C_1 should be one. For the discriminator 2 of both PMTs a threshold of -5V is chosen.

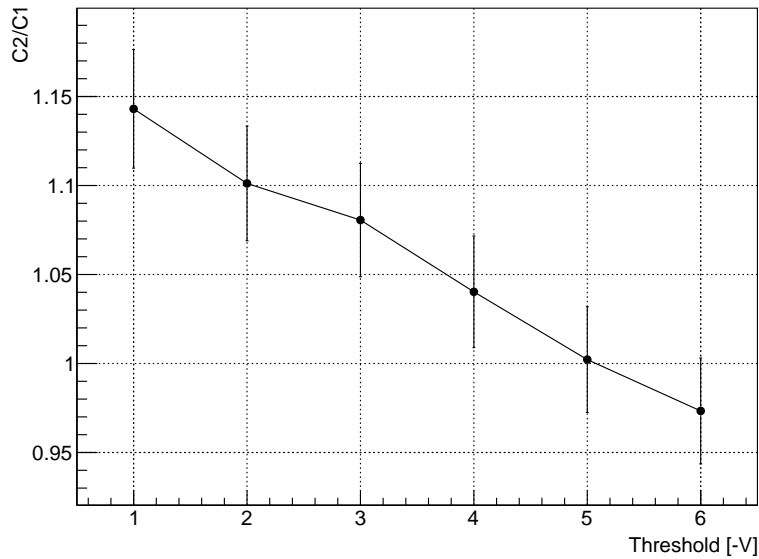


Figure 7.7: Threshold measurement for discriminator 2 of PMT 01. The ratio $C2/C1$ of the count rate after discriminator 1 ($C1$) and the rate after both discriminators ($C2$) is measured at different thresholds.

7.5 Adjusting the Delay Time

As mentioned in section 4.2 the time difference between a photon being generated in the fibres and the corresponding electrical signal in the SPIROC ASIC peaking is about 200ns. All the delays introduced through cables, processing time of the electronics and other factors are listed in table 7.1.

The delay time of the trigger electronics is measured between the first discriminator and the output of the NAND logic. To reach the desired value of 200ns a delay unit introducing a 30ns delay is used.

scintillation time	20ns
discriminator 1	7ns
cable	8ns
trigger electronics	141ns
delay unit	30ns
total delay time	206ns

Table 7.1: Delay times of the various processes and electronics.

7.6 Trigger Performance

A quick way to see if the trigger setup performs right is to check the coincidence rate. The two scintillation counters are arranged perpendicular to each other which results in a square trigger area of 100cm^2 . The rate of cosmic particles incident on the earth's surface is approximately $1\text{cm}^{-2}\text{min}^{-1}$ which means the coincidence rate should be 100min^{-1} .

The measured rate is 105.6min^{-1} and is close to the expected one, this ensures the trigger performs well.

7.7 Mechanical Installation

The whole setup is installed on a rack with additional holders for the scintillation counters and electronics. Figure 7.8 shows the trigger setup consisting of the two scintillation counters (orange) with their support structures (light grey) and the fibre module (yellow). The counters are arranged perpendicular to each other and are placed as close as possible to the fibre module.

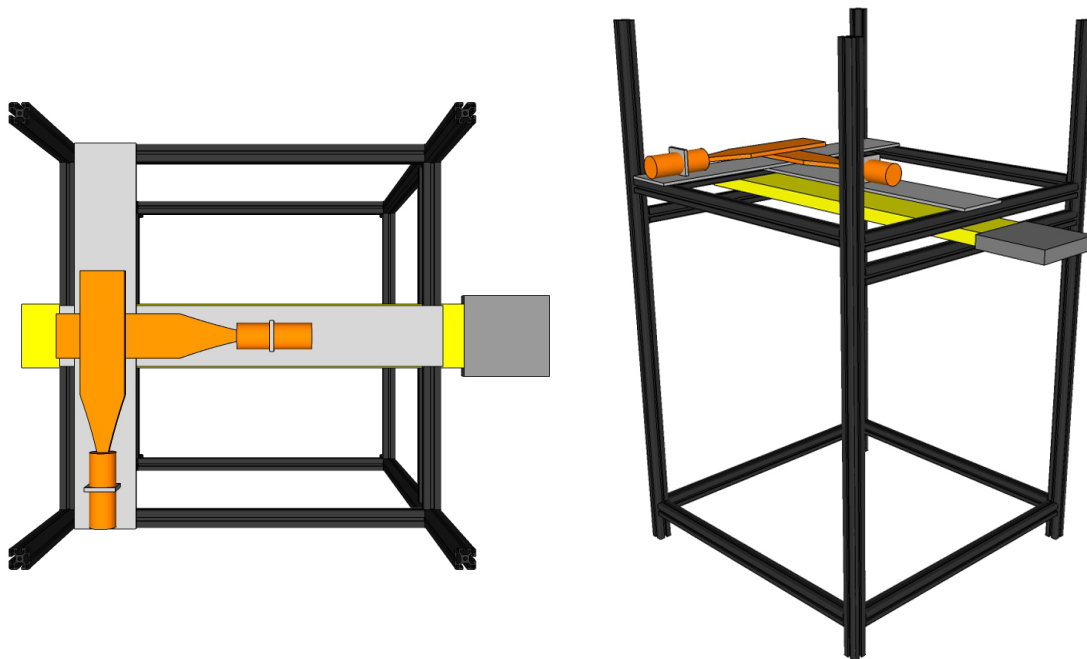


Figure 7.8: Schematic of the mechanical installation from different angles. The rack (black) supports the scintillation counters (orange) and the fibre module (yellow). The electronic readout is not shown.

8 Light Yield Measurement

In this chapter the analysis method and results for data taken with the cosmic setup are presented. First the short module is studied and used to determine whether the setup works correctly. After this is made sure, the 2.5m long module which has known damages is installed into the setup and examined.

The property of the modules which is investigated is the average photon yield per channel, called light yield.

8.1 Analysis Method

The first step of the data analysis is to convert the ADC values from each event into the number of detected photons using the following equation:

$$\#PhotoElectrons = \frac{ADC - Pedestal(channel)}{Gain(channel)/GainCorrection}$$

The pedestal and gain values for each channel are obtained from an LED calibration run. The *GainCorrection* is needed because the gain values obtained from LED and particle data differ slightly.

After the data is converted a cluster finding algorithm combines the signal of individual channels into clusters. This is necessary because a particle passing through the module will excite multiple fibres leading to a signal in more than one channel. Clustering in this case means to search for patterns in each event over the whole channel range and to combine the signals which come from one particle into one cluster.

The cluster algorithm used to find the clusters iterates over all channels. If the signal in a channel exceeds the neighbor threshold a cluster candidate is formed, it will then add up all the signals from the following channels until it finds a channel where the signal is below this threshold. A cluster candidate is accepted when its sum is over the sum threshold and the highest single channel signal exceeds the seed threshold. An illustration of the algorithm is given in Figure 8.1. To make sure the algorithm will neither combine clusters from two particles nor separate single particle clusters the thresholds have to be adjusted correctly. For the cosmic data the following thresholds in units of photo electrons (p.e.) are chosen:

- **Neighbor Threshold:** 1.5p.e.
- **Seed Threshold:** 2.5p.e.
- **Sum Threshold:** 4.5p.e.

To calculate the light yield the total charge of a cluster is assigned to the channel which corresponds to the position of the mean of the cluster charge distribution. For each channel this results in a distribution of the collected charge. The mean value of this distribution is the light yield and the error is given by its standard deviation.

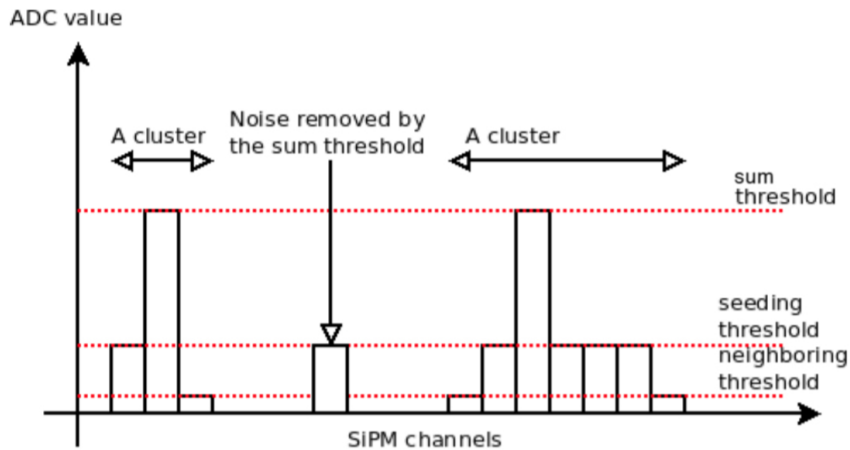


Figure 8.1: Illustration of the clustering algorithm. [4](edited)

8.2 Measurements of the 1m long Module

The first light yield measurement of the 1m long module can be seen in Figure 8.2. Dead channels are vetoed during analysis and therefore have a light yield of 0p.e. In the middle of each SiPM the light yield drops significantly due to the gap between the dies.

The light yield distribution also exhibits some other distinct features. Over the first 128 channels the light yield is around 30p.e. with a small drop to 26p.e. around channel 40. From channel 128 to 383 it then drops smoothly to 25p.e. At channel 384 there is a jump in the light yield back to 30p.e.

Figure 8.3 shows the distribution of clusters over the whole channel range. The number of clusters decreases at the edges which is probably due to inefficiency of the trigger and UV irradiation damage of the fibre mat. Also visible are the dead channels and the gaps between the SiPM dies.

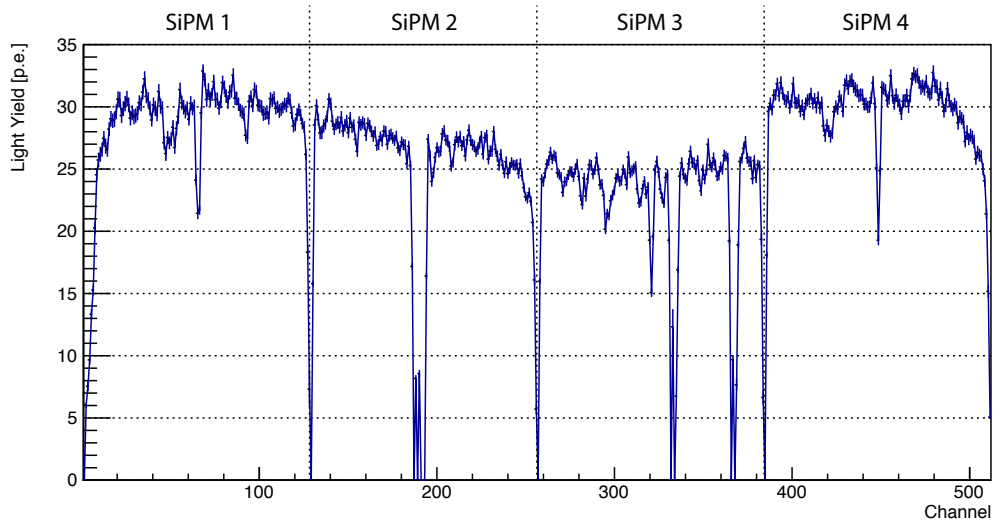


Figure 8.2: Light yield distribution of the 1m long module.

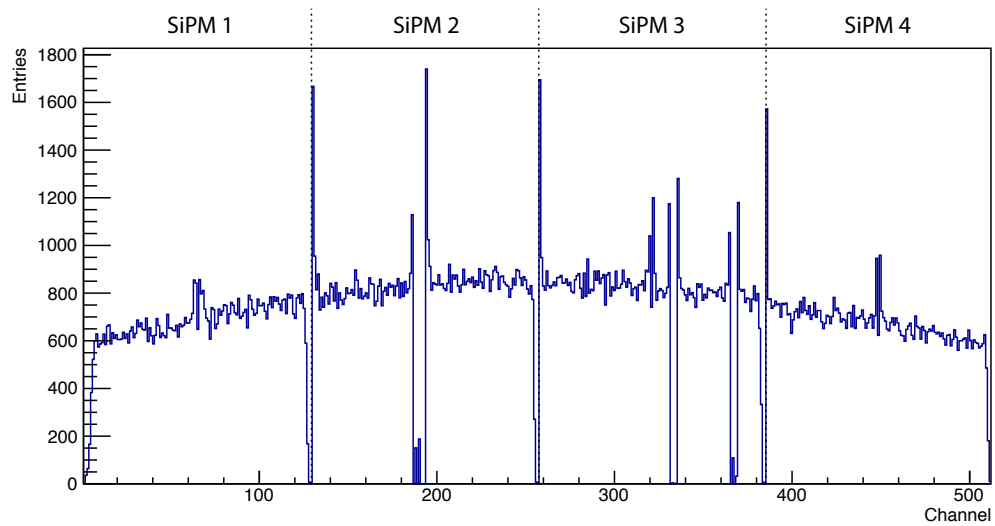


Figure 8.3: Distribution of the number of clusters detected in each channel. In a total of about 800,000 recorded events 375,000 clusters are found. This translates to an efficiency of about 47%.

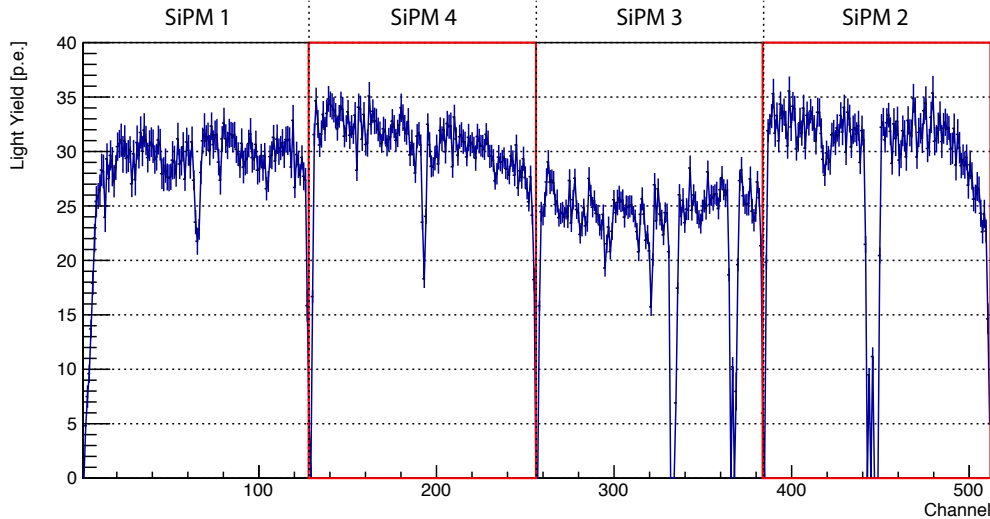


Figure 8.4: Light yield measurement after swapping the second and fourth SiPM. The swapped SiPMs are highlighted in red. The jump in light yield at channel 384 is still present.

To investigate where the jump at channel 384 is coming from, the second and fourth SiPM are swapped and another measurement is done. The result can be seen in Figure 8.4.

After swapping the SiPMs the light yield between channels 128 and 255 increased but the slope stayed the same. At the position of SiPM 2 the light yield also increased slightly which even pronounces the jump at channel 384. Since the jump is still present and the fact that the light yield changed slightly after the SiPMs have been reattached to the module, leads to the conclusion that the SiPMs are not aligned properly relative to each other. Therefore the holder which is used to attach the SiPMs to the module is replaced with a new one. In addition to the two screws which are used to attach each SiPMs, it now features two alignment pin holes which allow to insert pins for precise alignment. The new holder can be seen in Figure 8.5.

Using the new holder a third measurement is done and the resulting light yield distribution is shown in Figure 8.6. The jump is now gone and the whole distribution is a lot more uniform.

The measurements performed with the 1m long module illustrate the importance of a precise alignment of the SiPMs relative to each other. If they are not aligned properly the light yield can vary by as much as 5p.e. and possible damages to the module can not be detected.

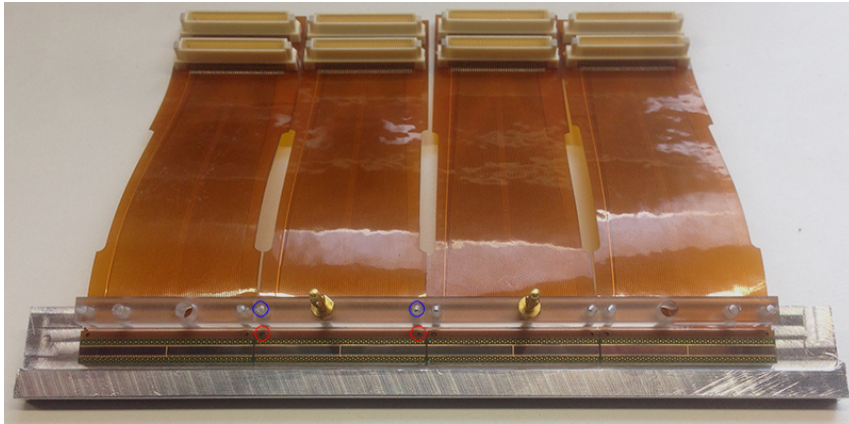


Figure 8.5: Picture of the new holder used to mount the SiPMs to the module. In addition to two screws (blue) it also features two alignment pins (red) to mount and precisely align the SiPMs. The old holder only consists of the clear plastic bar.

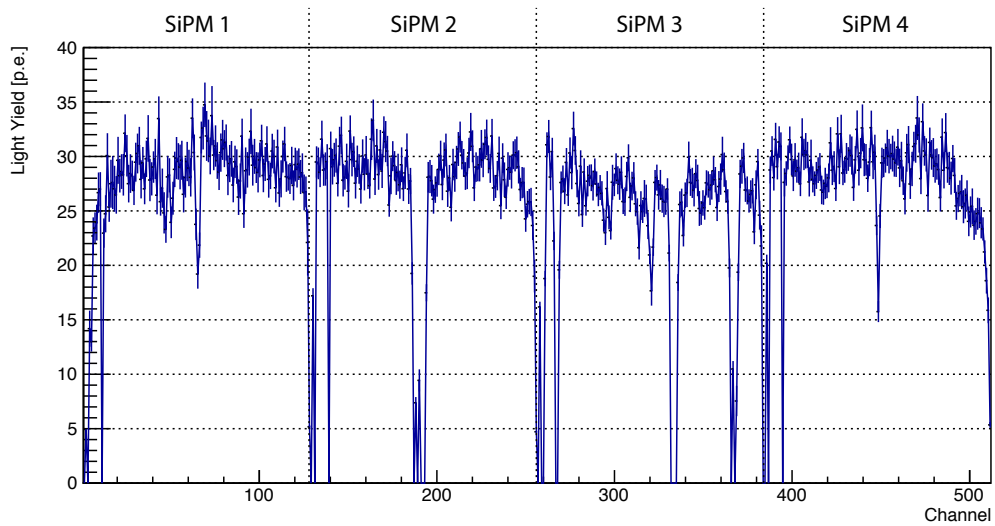


Figure 8.6: Light yield distribution of the 1m long module after precise alignment of the SiPMs. The large errors are due to low statistics.

8.3 Measurements of the 2.5m long Module

The light yield of the 2.5m long module is measured with different sources and trigger systems. The first measurement is done using the cosmic setup as described in this thesis. This data is then compared to data taken with a strontium-90 β -source and a different trigger system. The last measurement is then repeated with cosmic rays but uses the trigger system of the β -source measurement. All measurements are done at the same position, 40cm away from the mirror.

8.3.1 Measurement with Cosmic Rays

The light yield measured with cosmic rays can be seen in Figure 8.7. All of the known damages are visible. The part of the module missing the mirror has a light yield of about 15p.e. whereas the part with mirror has light yield of 22p.e. Due to the radiation damage the light yield decreases from 22p.e. to 14p.e. with mirror and to 12p.e. without the mirror. Also visible is an about 30 channels wide and 4p.e. deep drop in light yield due to a broken alignment pin.

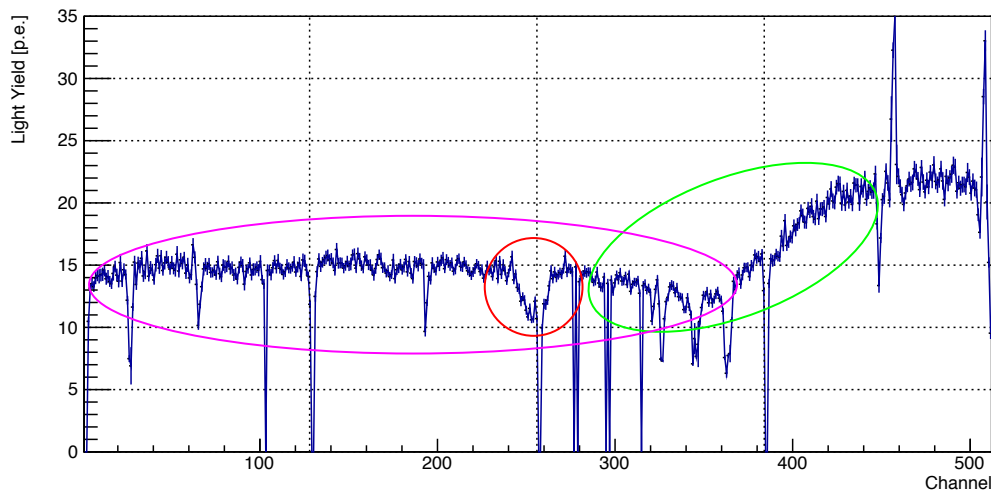


Figure 8.7: Light yield of the 2.5 long module measured with cosmic rays. Purple: missing mirror. Green: radiation damage. Red: broken alignment pin.

8.3.2 Measurement with a β -Source

For this measurement the setup is changed slightly. The two scintillation counters are replaced by a smaller trigger setup that is mounted beneath the module. Since the β -source is collimated it is placed at four positions along the width of the module to ensure that there are enough clusters in all channels. The setup is illustrated in Figure 8.8.

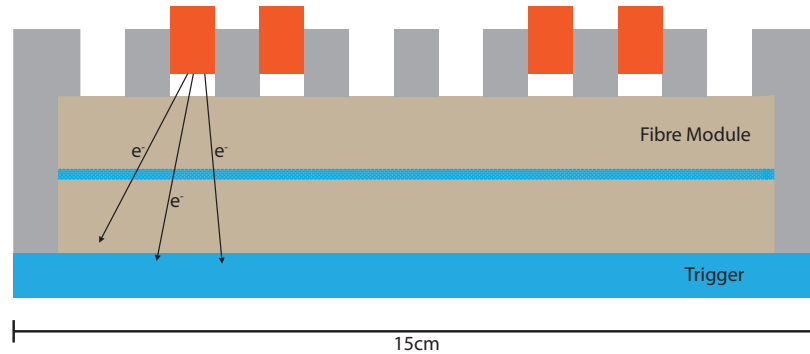


Figure 8.8: Schematic of the setup used for the measurement with the β -source. The source (orange) is placed at four positions inside the metal holder (grey). The trigger is positioned beneath the module.

Figure 8.9 shows the light yield measurement taken with the β -source and the measurement from section 8.3.1. Both histograms have nearly identical profiles and show the damages of the fibre module. The ratio of the normalized histograms is around 1 which means that both measurements are consistent with each other. The light yield from β -particles is mostly about 2p.e. to 3p.e. lower than the one from cosmic rays. The regions with lower light yield coincide with the positions of the β -source where the electrons are highly collimated and thus produce smaller cluster than electrons emitted under a bigger angle. A comparison of the cluster sizes can be seen in Figure 8.10. The discrepancy in light yield can not be explained from the acquired data alone and was not further studied.

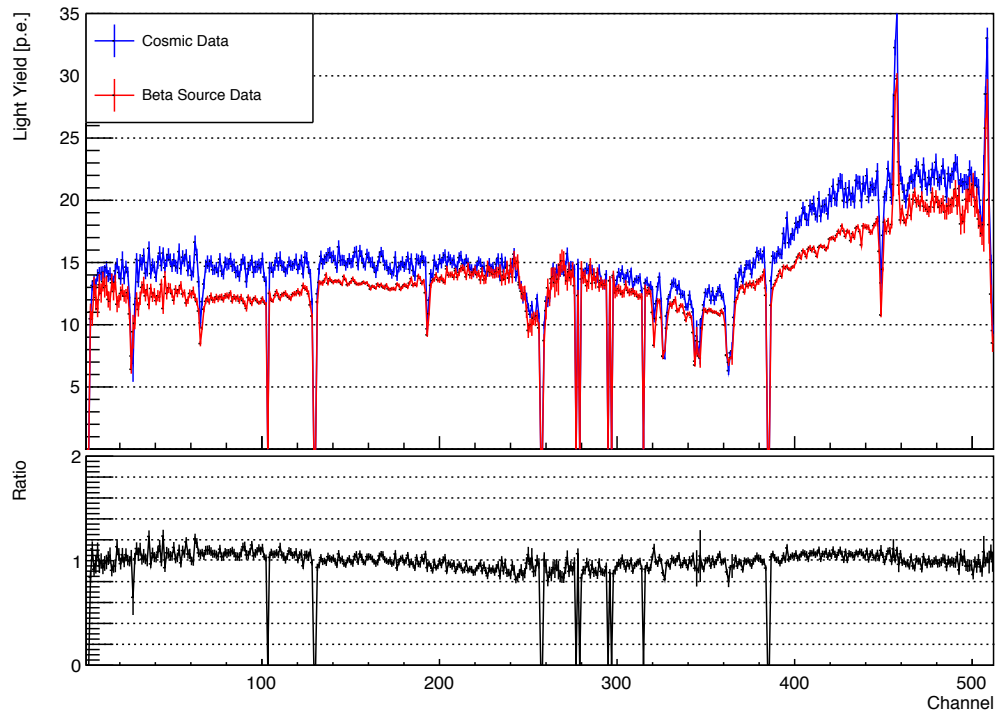


Figure 8.9: Comparison of the light yield curves taken with cosmic rays and a β -source. The ratio of the normalized histograms is around 1, which verifies that cosmic rays can be used for quality assurance of fibre modules.

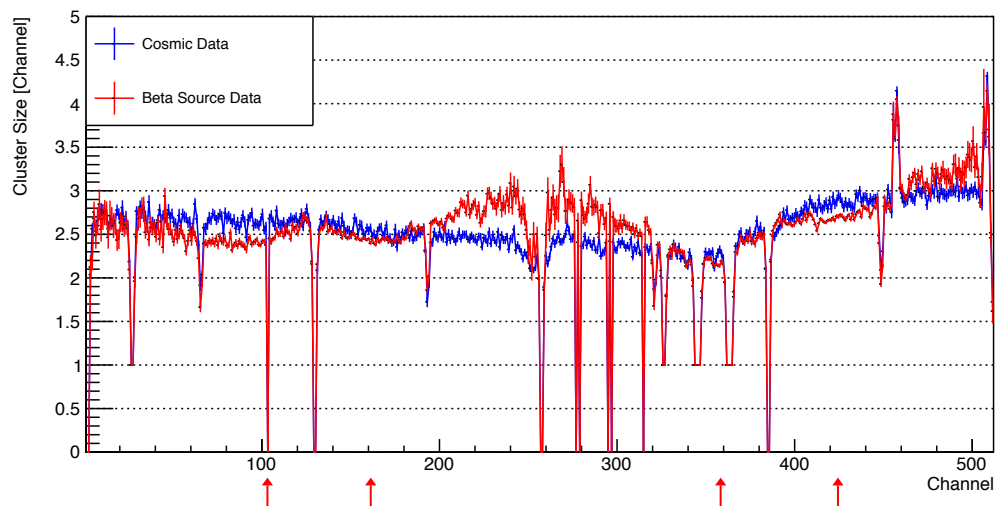


Figure 8.10: Comparison of the cluster size from cosmic rays and a β -source. The red arrows indicate the position of the source.

8.3.3 Measurement with Cosmic Rays and β -Source Trigger

The trigger used for the measurement with the β -source is now used to trigger on cosmic particles to check whether it can be used for further measurements.

The trigger despite its smaller area of $1\text{cm}\times 15\text{cm}$ compared to the $10\text{cm}\times 10\text{cm}$ of the original trigger exhibits the same trigger rate of about 100min^{-1} . Usually one would expect a rate of 15min^{-1} . The high trigger rate indicates that there is a lot of false triggers.

In about 150,000 events recorded over the course of 25 hours, 19,000 clusters are found which results in an efficiency of 13%. This proves that indeed most of the trigger signals are false triggers.

Figure 8.12 shows that only about 30 to 40 clusters per channel are found. This results in the large statistical error of the light yield shown in Figure 8.11. Despite the large errors all of the module's damages are visible. A measurement over two days has not been done during this thesis due to time limitations.

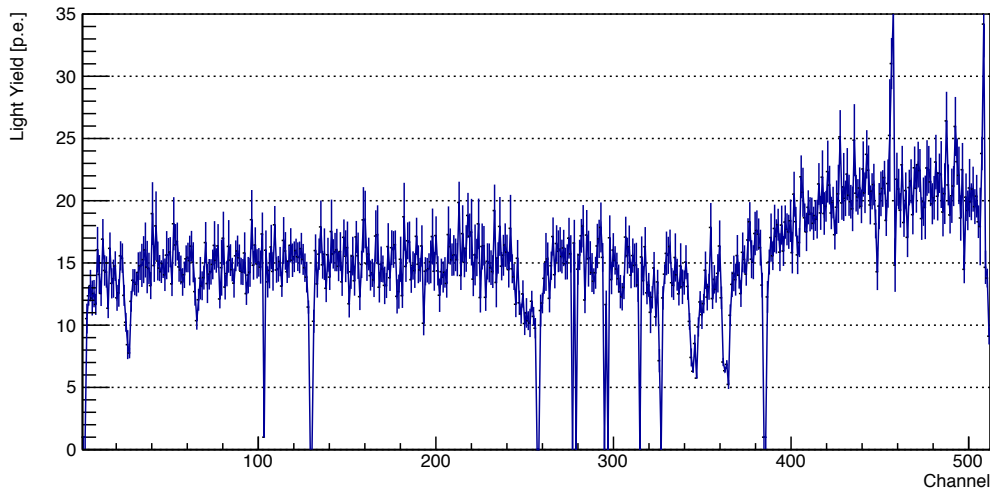


Figure 8.11: Light yield measured with cosmic rays and the trigger usually used for the β -source. The large errors are due to low statistics.

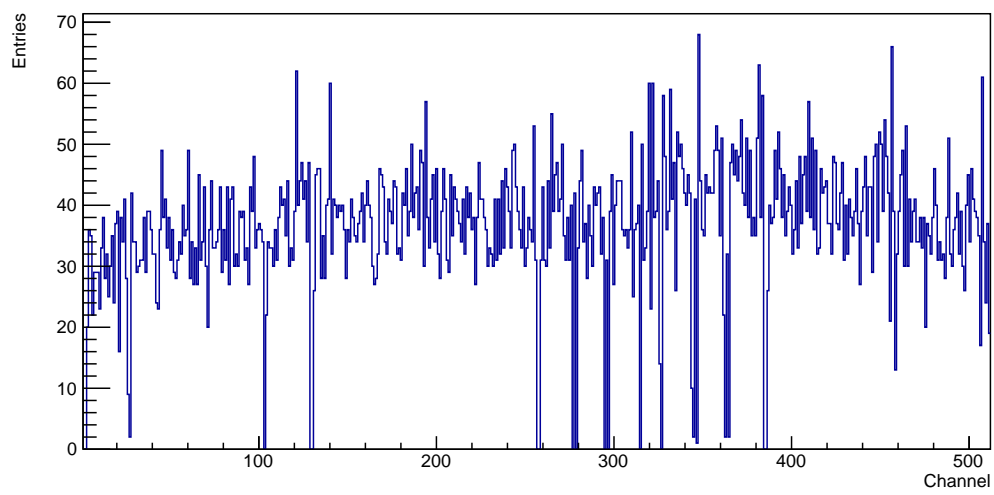


Figure 8.12: Distribution of the number of clusters detected in each channel. In a total of about 150,000 recorded events 19,000 clusters are found, resulting in an efficiency of 13%.

9 Summary and Outlook

A forward tracking system build out of scintillating fibres, which will be readout by silicon photomultipliers (SiPMs), will be one of the major components of the currently ongoing upgrade of the LHCb experiment. The tracking system consists of twelve layers, which in turn consist of twelve modules of the size of $52\text{cm} \times 5\text{m}$. Each module is readout by 32 SiPMs. In the course of this thesis a setup for quality assurance of the fibre modules with cosmic rays has been commissioned.

To ensure a uniform electric response a calibration routine is developed which allows to operate all SiPM channels at the same over voltage. The achieved stability is of the same order of magnitude as fluctuations caused by temperature changes of 1K in the laboratory.

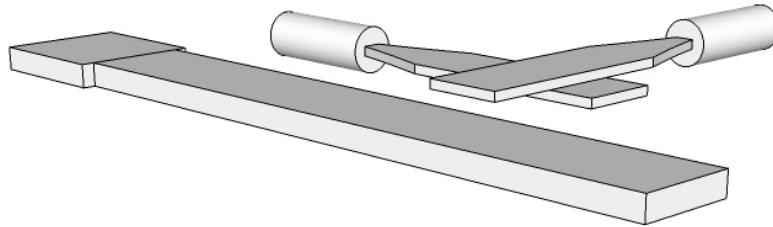


Figure 9.1: Illustration of the trigger setup. The two scintillation counters sit on top of the module.

The system used to trigger on cosmic rays consists of two scintillation counters which form a coincidence. Both counters are placed on top of the module. The two counters have an overlapping area of 100cm^2 and a trigger rate of around 100min^{-1} which is what one would expect given the geometry. In about 50% of the triggered events a signal is found. The number of found signals could be increased by placing one scintillation counter on top of the module and the other one below it. This would make sure a trigger signal is only given for particles passing through the module. Due to mechanical constraints this geometry could not be realized without decreasing the trigger rate significantly.

Using the setup the light yield of a 1m long one, and a 2.5m long module has been studied. Both modules are 13cm wide and readout by four SiPMs. The light yield measurements of the 1m long module show the importance of precisely aligning the SiPMs such that they are neither tilted nor offset to one another. Otherwise drops in light yield due to poor quality or damages of the module are not visible.

The light yield of the 2.5m long module is measured with cosmic rays and also with a strontium-90 β -source. For the β -source a different trigger system is used, it sits below the module and has an active area of $1\text{cm} \times 15\text{cm}$. This trigger is then also

used to trigger on cosmic rays.

The measurements verify that quality assurance with cosmic rays is possible, and that the obtained light yields are consistent with measurements done with a β -source. The slight difference in light yield between data from cosmic rays and from β -particles was not studied further in this thesis. This is not an issue for quality assurance with cosmic rays. Measurements of new modules can be compared to a reference module which exhibits an ideal light yield.

The measurement with the trigger system originally designed for the β -source shows that the system can, in principle, also be used to trigger on cosmic rays if data is taken over the course of two days. It also shows that, due to the low flux of cosmic rays, $I = 1\text{cm}^{-2}\text{min}^{-1}$, a large enough and efficient trigger is necessary. Otherwise the statistics are too low to confidently characterize a module within a reasonable amount of time.

The measurements that have been carried out in this thesis prove that quality assurance of fibre modules can be done using cosmic rays. For the quality control of the final modules the setup needs to be extended to accommodate their larger dimensions.

10 References

- [1] Philippe Mouche. Overall view of the LHC. Vue d'ensemble du LHC. General Photo, Jun 2014.
- [2] Alves et al. The LHCb Detector at the LHC. *J. Instrum.*, 3(LHCb-DP-2008-001. CERN-LHCb-DP-2008-001):S08005, 2008. Also published by CERN Geneva in 2010.
- [3] Rolf Lindner. LHCb layout2. LHCb schema2. LHCb Collection., Feb 2008.
- [4] LHCb Collaboration. LHCb Tracker Upgrade Technical Design Report. Technical Report CERN-LHCC-2014-001. LHCb-TDR-015, CERN, Geneva, Feb 2014.
- [5] Christian Joram, Ulrich Uwer, Blake Dean Leverington, Thomas Kirn, Sebastian Bachmann, Robert Jan Ekelhof, and Janine Mueller. LHCb Scintillating Fibre Tracker Engineering Design Review Report: Fibres, Mats and Modules. Technical Report LHCb-PUB-2015-008. CERN-LHCb-PUB-2015-008, CERN, Geneva, Mar 2015.
- [6] T.O. White. Scintillating fibres. *Nuclear Instruments and Methods in Physics Research Section A: Accelerators, Spectrometers, Detectors and Associated Equipment*, 273(2):820 – 825, 1988.
- [7] Blake Dean Leverington. The LHCb upgrade and the Scintillating Fibre Tracker. Jul 2015.
- [8] Wolfgang Demtröder. *Experimentalphysik 3, Atome, Moleküle und Festkörper*. Springer-Lehrbuch, ISBN: 978-3-540-21473-1 (Print) 978-3-540-27411-7 (Online), 2005.
- [9] Norbert Kolanoski, Hermann Wermes. *Teilchendetektoren, Grundlagen und Anwendungen*. Springer-Lehrbuch, ISBN: 978-3-662-45349-0 (Print) 978-3-662-45350-6 (Online), 2016.
- [10] Axel Kuonen, Olivier Girard, and Guido Haefeli. Characterisation of the Hamamatsu MPPC multichannel array for LHCb SciFi Tracker v.9.2014. Technical Report LHCb-INT-2015-004. CERN-LHCb-INT-2015-004, CERN, Geneva, Feb 2015.
- [11] Orsay Micro Electronics Group Associated (OMEGA). Spiroc-a draft: Datasheet. Version 27, December 2009.

- [12] Wolfgang Demtröder. *Experimentalphysik 4, Kern-, Teilchen- und Astrophysik*. Springer-Lehrbuch, ISBN: 978-3-642-21475-2 (Print) 978-3-642-21476-9 (Online), 2014.
- [13] Peter Biermann and Gunter Sigl. Introduction to cosmic rays. *Lect. Notes Phys.*, 576:1–26, 2001. [,1(2002)].

A Appendix

A.1 Additional Figures

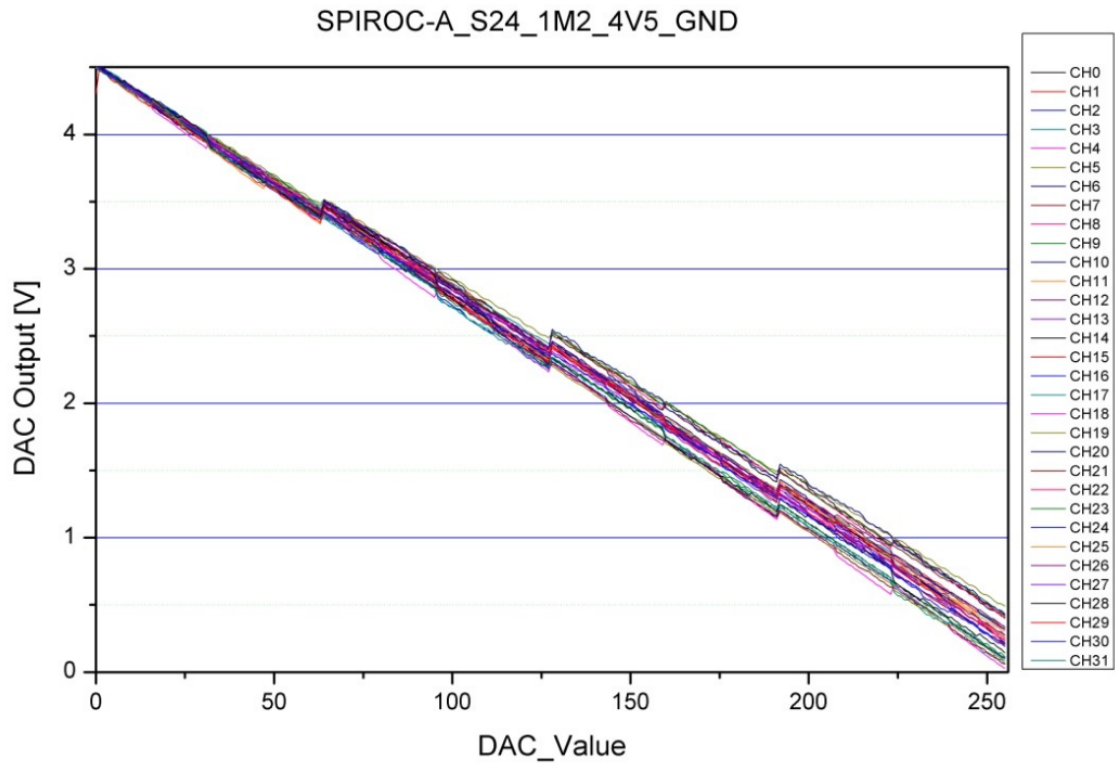
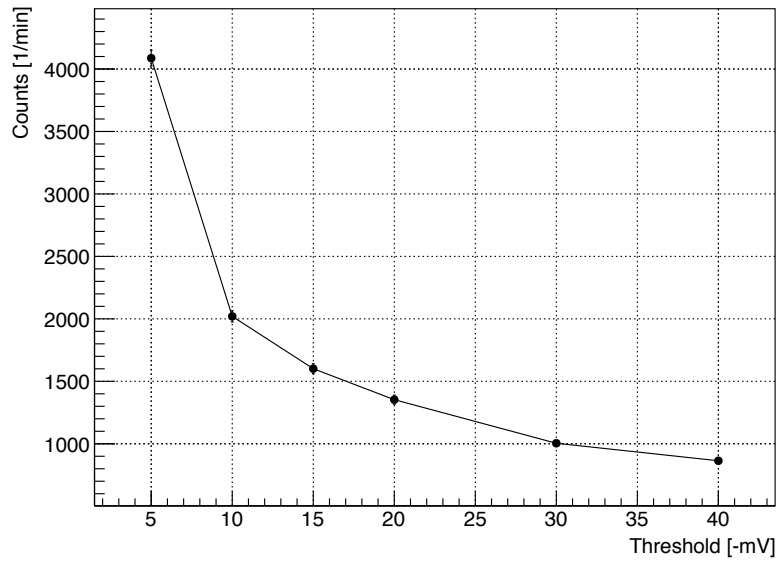
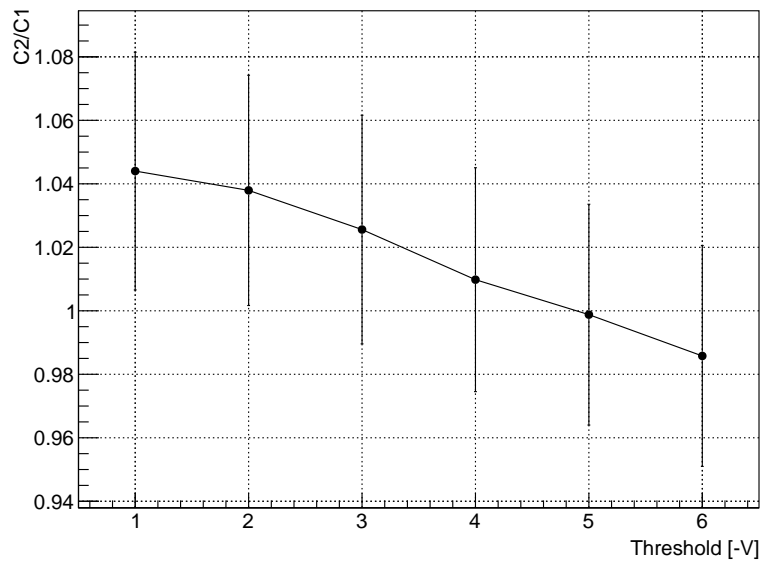


Figure A.1: SPIROC DAC output. Highly non monotonic over the whole DAC-range. Taken from: http://indico.cern.ch/event/118266/contribution/13/attachments/59713/85823/SPIROCA_10.01.11.pdf



(a) Discriminator 1



(b) Discriminator 2

Figure A.2: Threshold measurement for the two discriminators of PMT 03. a) The count rate was measured as a function of the threshold. b) The ratio $C2/C1$ of the count rate after discriminator 1 ($C1$) and the rate after both discriminators ($C2$) at different thresholds.

Erklärung:

Ich versichere, dass ich diese Arbeit selbstständig verfasst habe und keine anderen als die angegebenen Quellen und Hilfsmittel benutzt habe.

Heidelberg, den 02.04.2016

.....